DIPLOMARBEIT

Titel der Diplomarbeit

"Phase transformations in Ni-Mn-Ga ferromagnetic shape memory alloys subjected to high pressure torsion"

Verfasser

Arno Emanuel Kompatscher

angestrebter akademischer Grad

Magister der Naturwissenschaften (Mag.rer.nat.)

Wien, im Juli 2012

Für meine Eltern:

Brigitte und Peter.

Love is wise, hatred is foolish.
Bertrand Russell

Abstract

Shape memory alloys (SMA's) are scientifically and technologically of high interest. In the course of this diploma thesis the ferromagnetic SMA $Ni_{54}Mn_{25}Ga_{21}$ was analysed. The aim of this work was to investigate the effect of the grain size on the martensitic phase transformation. To reach a grain size of about 100 nm the material was subjected to high pressure torsion (HPT) to a degree of deformation of up to $6 \cdot 10^5$ %. Before and after HPT as well as after HPT and subsequent heat treatment a systematic analysis via transmission electron microscopy (TEM), differential scanning calorimetry (DSC) and X-ray diffraction (XRD) was conducted. The experimental results show that the grain size before HPT is in the range of several hundreds of micrometres. The crystalline structure of the coarsed grains was identified as unmodulated tetragonal 2M-martensite. HPT induced strong fragmentation of the grains mainly by the formation of subgrain boundaries. The resulting submicrocrystalline structure contains a face centered tetragonal structure (fct) which originates from the chemical disordering of the martensitic 2M phase. HPT also induces a structural transformation since a disordered face centered cubic γ-phase (fcc) arises additionally after deformation. Due to the strong chemical disorder and the occurrence of the fcc γ-phase the thermally induced martensitic back transformation to austenite is completely suppressed. Isochronal heating on the other hand initially shows a phase transformation from fcc/fct to bcc (disordered body centered cubic). This process ends at a temperature of about 420 °C. After further isochronal heating to 500 °C the bcc phase transforms into the austenitic Heusler-phase via chemical ordering. The average diameter of the grains was observed to be around 140 ± 6 nm.

Upon cooling the martensitic phase transformation returns in the small grains. How-

ever due to the influence of the small grain size the austenite transforms into the modulated 7M structure of the martensite. The occurrence of the metastable 7M phase at the account of the 2M equilibrium structure can be explained by the influence of grain size on the free enthalpy of the 2M phase. In small grains the 7M structure optimally accommodates the transformation strains. A central result of this work is that for the first time the model of an adaptive structure of the martensite was successfully used as a physical interpretation for the stabilization of the 7M phase in small grains.

Zusammenfassung

Formgedächtnislegierungen (SMA's) sind wissenschaftlich und technologisch von großem Interesse. Im Rahmen dieser Diplomarbeit wurde die ferromagnetische SMA $Ni_{54}Mn_{25}Ga_{21}$ untersucht. Ziel war es, den Effekt der Korngröße auf die martensitische Phasentransformation zu untersuchen. Um eine Verkleinerung der Körner bis in den Bereich von rund 100 nm zu erzielen wurde das Material durch Hochdrucktorsion (HPT) bis zu einem Deformationsgrad von $6 \cdot 10^5$ % verformt. Vor und nach Hochdruckverformung, sowie nach HPT und anschließender Wärmebehandlung wurden in systematischer Weise Untersuchungen mittels Transmissionselektronenmikroskopie, Differentialrasterkalorimetrie sowie Röntgenbeugung durchgeführt.

Als Ergebnis der Experimente zeigt sich, dass die Korngröße vor HPT im Bereich von mehreren hundert Mikrometern liegt. Die kristalline Struktur der groben Körner wurde als geordneter nichtmodulierter tetragonaler 2M-Martensit identifiziert. Hochdrucktorsion induzierte eine starke Fragmentierung der Körner hauptsächlich durch die Bildung von Subkorngrenzen. Die entstehende submikrokristalline Struktur enthält eine ungeordnete fct Struktur, die durch chemischen Entordnung der martensitischen 2M Phase entsteht. HPT induziert ebenso eine strukturelle Transformation, da nach der Hochdeformation auch die ungeordnete fcc-Gammaphase auftritt. Durch die starke chemische Entordnung und durch die die Bildung der fcc Phase wird die thermisch induzierte martensitischen Rückumwandlung zum Austenit vollständig unterdrückt. Hingegen tritt durch isochrones Heizen zunächst eine Phasenumwandlung fcc/fct nach bcc (ungeordnet kubisch raumzentriert) auf. Dieser Prozess ist bei einer Temperatur von rund 420 °C abgeschlossen. Nach weiterem isochronen Heizen bis zu einer Temperatur von 500 °C wandelt die bcc Struktur durch die Einstellung chemischer Ordnung in die austenitsche Heusler-Phase um.

Hingegen findet durch diese Wärmebehandlung kein nennenswertes Kornwachstum statt (die durchschnittliche Korngröße liegt bei ca. 140 ± 6 nm).

In den kleinen Körner tritt beim Abkühlen wieder eine martensitische Phasenumwandlung auf. Allerdings wandelt durch den Einfluss der kleinen Korngröße der Austenit in die modulierte 7M Struktur des Martensits um. Das Auftreten der metastabilen 7M Phase auf Kosten der 2M Gleichgewichtsstruktur wird durch den Einfluss der Korngröße auf die freie Enthalpie der 2M Phase erklärt. In kleinen Körnern ermöglicht die 7M Struktur eine optimale Akkommodation der Umwandlungsverzerrungen. Ein zentrales Ergebnis dieser Arbeit ist, dass das Modell einer adaptiven Struktur des Martensits erstmals erfolgreich für die physikalische Interpretation der Stabilisierung der 7M Phase in kleinen Körner angewandt wurde.

List of Abbreviations

$\mathbf{A_s}$, $\mathbf{A_p}$, $\mathbf{A_f}$	Austenite start, peak and finish temperature
bcc	body centered cubic (lattice)
BF	Bright Field (imaging)
DF	Dark Field (imaging)
DSC	Differential Scanning Calorimetry/Calorimeter
fcc	face centered cubic (lattice)
fct	face centered tetragonal (lattice)
(F)SMA	(Ferromagnetic) Shape Memory Alloy
(F)SME	(Ferromagnetic) Shape Memory Effect
Ga	Gallium, element no. 31 in the periodic table
$\mathbf{H}$, $\mathbf{\Delta H}$	Enthalpy, change of Enthalpy
HPT	High Pressure Torsion
HT	Heat treatment
Mn	Manganese, element no. 25 in the periodic table
$\mathbf{M_s}$, $\mathbf{M_p}$, $\mathbf{M_f}$	Martensite start, peak and finish temperaure
Ni	Nickel, element no. 28 in the periodic table
RT	Room temperature
SAD	Selected Area Diffraction
SPD	Severe Plastic Deformation
$\mathbf{T_C}$	Curie temperaure
TEM	Transmission Electron Microscopy/Microscope
XRD	X-Ray Diffraction

Contents

Chapter I

Introduction

Shape memory alloys (SMA) have come to higher attention in recent years. These materials have unique thermomechanical properties. If deformed in the martensitic phase they exhibit a macroscopic shape change upon heating through a reverse martensitic transformation. That is: a martensitic phase of lower crystallographic symmetry undergoes a phase transformation to an austenitic phase of higher crystallographic symmetry. There are three distinct phenomena associated with the shape memory effect (SME)[1, 2]: *firstly* the temperature driven SME, where the shape is retrieved after heating above the temperature, where the reverse martensitic transformation (martensite $\rightarrow$ austenite) takes place. The strains in this case are in the range of about 10%. *Secondly* the superelastic effect or simply superelasticity, where an applied external force causes a forward martensitic transformation (austenite $\rightarrow$ martensite). When the force is released the reverse martensitic transformation causes a reversion to the original shape. This effect is usually observed at higher temperatures well within the austenitic phase. The strains go up to 18%[3]. *Thirdly* the magnetically driven SME or ferrmomagnetic SME (FSME), where an internal rearrangement of twins in the martensitic phase is achived via the application of an external magnetic field. Strains go as far as 10%. The FSME is significantly faster than the temperature driven SME, which makes it especially interesting for a number of applications such as actuators e.g. for pumps. The FSME is also of special interest for this work, since the alloy studied in the present work is the $Ni_{54}Mn_{25}Ga_{21}$ ferromagnetic shape memory alloy (FSMA).

Grain size plays a vital role in martensitic phase transformations and influences the behaviour of shape memory materials[4]. The aim of this work was to research the effects of a small grain size on the $Ni_{54}Mn_{25}Ga_{21}$-FSMA. The material was analyzed in it's coarse grained state with grain sizes of several hundreds of μm as well as in ultrafine grained state with grain sizes in the range of 140 nm. To reach this strong decrease of grain size the alloy was subjected to severe plastic deformation (SPD) via high pressure torsion (HPT). Analyses were performed by means of transmission electron microscopy (TEM), x-ray diffraction (XRD) as well as differential scanning calorimetry (DSC).

I.1   Structure

This thesis is divided into six main chapters.

- In this, the first chapter, a short introduction is given into the *Why* and the *What* and a a general outline of the results.

- In the second chapter the theoretical framework about crystallography and martensitic transformations is given.

- The third chapter describes the experimental procedures and methods used and as to why they were used.

- The fourth chapter deals with the experimental results and gives a detailed account of the experimental data gathered during the research for this thesis.

- In the fifth chapter an interpretation of the gathered data is presented in the light of recent and past literature on the matter.

- Finally a summary and short conclusions are given in the sixth chapter.

Chapter II

Theoretical Framework

II.1 Martensitic Phase Transformations & Shape Memory Effect

A martensitic transformation is a displacive, diffusionless first order phase transformation found in solids. It's kinetics and morphologhy are dominated by strain energy[5]. Martensite is named after the German metallurgist Adolf Martens (1850 - 1914), who first observed it in steels. In solids exhibiting martensitic phase transformations there are two distinct phases: a high temperature - usually cubic - parent phase: the so called austenite. And secondly a low temperature phase typically of lower symmetry called the martensite[3]. When the temperature is lowered to the martensite start temperature $\mathbf{M_s}$, the so called martensitic transformation starts. Because of the lower symmetry of the martensitic phase, there are several different variants of the same structure that can arise (e.g. A and B in Figure II.1). If heated back to another characteristic temperature - the austenite start temperature $\mathbf{A_s}$ - the martensite becomes unstable and reverts to the austenitic phase. Based on the reversible transformation between the austenite and the martensite unique thermomechanical effects - such as the shape memory effect of the superelastic effect - arise. The transformation is dominated by a collective shearing of the atoms. Although the relative movements on the atomic scale are small, the summation of all shifts can lead to a reversible shape change on the macroscopic scale[3].
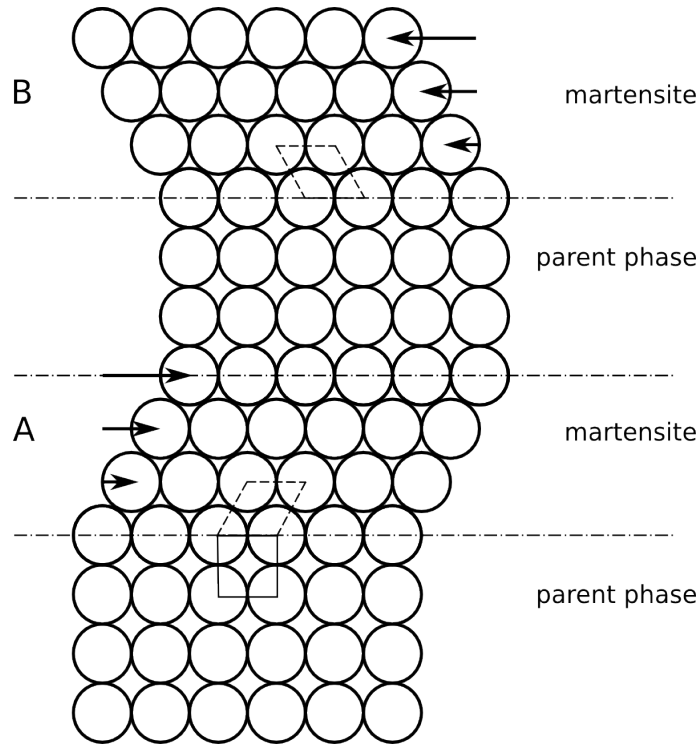
Figure II.1: Simplified model of a martensitic phase transformation. Adapted from [3], Fig. 1.2.

II.1.1   Ferromagnetic Shape Memory Effect (FSME)

The temperature driven SME is a comparatively slow effect only in the range of 1 Hz . This is due to thermodynamical limiting factors influencing heat flow (e.g. the coefficient of heat conductivity, which is material specific). For many applications it would be preferable to have a significantly faster process of shape change (in the range of several hundreds of Hz). To this end ferromagnetic alloys with a martensitic transformation can be used, as they exhibit the *ferromagnetic* SME[1, 2]. Among these alloys are Fe-Pd[6], La-Sr-CuO$_4$[7], Co-Ni-Ga[8] as well as the one presented in this work: Ni-Mn-Ga[2, 9].

In ferromagnetic materials where no external magnetic field is applied, there is the *easy direction*: the preferred direction of magnetization. In a material with a twinned microstructure, the twins have different crystallographic orientations. If the easy direction is parallel to the crystallographic orientations of the respective twins, then the magnetization directions differ (arrows in Figure II.2a). If an external field is applied and the energy needed to realign the magnetic moment is higher than that to

move a twin, the twin boundary will move and the twins with magnetic orientation parallel to the magnetic field will grow at the account of the other variant (see Figure II.2b)[1].

It is especially important to note that the FSME is caused by an *internal twin rearrangement* of the martensite whereas the temperature driven SME is caused by the phase transformation from the crystallographically lower symmetric martensite to the austenite of higher crystallographic symmetry. In any case these processes have to be crystallographically reversible in order for the SME to occur.
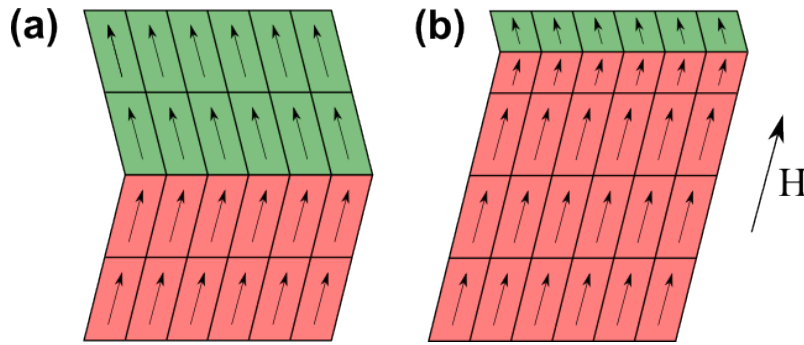

Figure II.2: Ferromagnetic shape memory effect (FSME). **(a)** Magnetic moments without the external field. **(b)** Redistribution of the variants in an applied field. Adapted from Ref. [1], Fig. 2.

II.2 Crystallography

During the course of this work several crystal structures were observed. There are a number of textbooks on the matter of crystallography introducing the concepts of crystal symmetry and space groups such as Ref. [10] or Ref. [11]. In this context the specific structures of Ni-Mn-Ga encountered via TEM and X-ray analysis are described as follows.

Six phases were observed:

- The high temperature phase: L2$_1$ Heusler **austenite** (space group Fm$\bar{3}$m Figure II.3(a))

- The low temperature phase: unmodulated 2M tetragonal martensite (space group I4/mmm, Figure II.3(b))

- disordered face centered tetragonal (disordered 2M martensite)

- γ-phase (disordered face centered cubic (fcc, space group Fm$\overline{3}$m))

- disordered body centered cubic (bcc, space group Im$\overline{3}$m)

- The thermodynamically metastable phase: modulated 7M martensite (Figure II.4 left); space group P2/m; to account for the modulation a superspace approach can be applied[12]

An excellent overview of Heusler alloys is given in Ref. [13]. The original nomenclature of a Heusler alloy was that of three different elements in a 2:1:1 stoichiometric composition (X_2YZ, where X, Y & Z are elements). An interesting property of Heusler alloys is that they can be ferromagnetic, although the comprising elements aren't necessarily ferromagnetic by themselves. The exact lattice parameter of the austenite of the specific composition $Ni_{54}Mn_{25}Ga_{21}$ was not found even after extended search in litearature. However the parameter of the similar composition $Ni_{53}Mn_{22}Ga_{25}$ is $a = 0.581$ nm[14].

Tetragonal martensite is the thermodynamically stable phase at low temperatures. It should be noted that in literature, the unmodulated 2M tetragonal structure is occasionally described via an orthorombic unit cell[15]. In this work the tetragonal characterization will be used. Transformation from L2$_1$ Heusler austenite to tetragonal martensite as illustrated in Figure II.3 is reached via compression in the (austenite's) a- and b-directions and elongation in the c-direction. The typical change lattice parameters and volume of similar stoichiometric compositions were ascertained as follows: a and b decrease at about 5%, c increases at about 12% and the overall volume change is only at about 2-3‰[14].

Based on the the unit cell depicted in Figure II.3(c) (half of the unit cell in Figure II.3(b)), a complete disordering of the 2M martensite would yield a face centred tetragonal lattice. Alternatively, the complete disordering might also be described by a body centred tetragonal (bct) lattice structure with a unit cell that is only a

quater of that of the ordered 2M lattice (Figure II.3(d)). In Table II.1 a comparison of the directions and lengths of the base vectors of the corresponding unit cells can be seen. They are expressed in the notation of the 2M unmodulated tetragonal martensite as illustrated in Figure II.3(b). For convenience the unit cell of the unmodulated 2M tetragonal martensite (indexed "2M" throughout the text, Figure II.3(b)) was also used to describe the disordered fct structure. It should be noted that disordering can cause slight changes in the lattice parameters.

	A	**fct**	**bct**
$[100]$	$\sqrt{2}[110]_{2M}$	$[100]_{2M}$	$\sqrt{2}/2[110]_{2M}$
$[010]$	$\sqrt{2}[0\bar{1}0]_{2M}$	$[010]_{2M}$	$\sqrt{2}/2[1\bar{1}0]_{2M}$
$[001]$	$[001]_{2M}$	$1/2[001]_{2M}$	$1/2[001]_{2M}$

Table II.1: Directions and lenghts of the base vectors of the corresponding unit cells in the notation of the face centered tetragonal cell of the 2M unmodulated tetragonal martensite. For illustration see Figure II.3. **A** austenite. **fct** face centered tetragonal. **bct** body centered tetragonal.

The dashed lines in Figure II.3(a) indicate the unit cell of the unmodulated 2M tetragonal martensite (Figure II.3(b)) with the aforementioned changes, specifically: $[110]_A \rightarrow [100]_{2M}$, $[1\bar{1}0]_A \rightarrow [010]_{2M}$ and $[001]_A \rightarrow [001]_{2M}$ (see also Table II.1). The tetragonal unit cell of the 2M martensite can be seen as simple stacking sequence A-B-A-B-... of the $(200)_{2M}$ planes. The 7M and 5M structures respectively show a more complex order of stacking, denoted as $(5\bar{2})$ and $(3\bar{2})$ after Zhdanov's notation as used by Pons et al.[16] (see Figure II.4). It should be noted that besides of the stacking order the specific chemistry of the different layers has to be considered yielding a doubling of the unit cell. Therefore 7M and 5M are sometimes referred to as 14M and 10M with $(5 \, overline2)_2$ and $(3\bar{2})_2$ in literature[17, 18]. To account for the full and complex superstructure of the 7M and 5M martensite additional shifts of the layers have to be considered. These shifts cause a sinusoidal modulated structure that might be incommensurate with the seven or five layered stacking sequence[12, 19, 20].
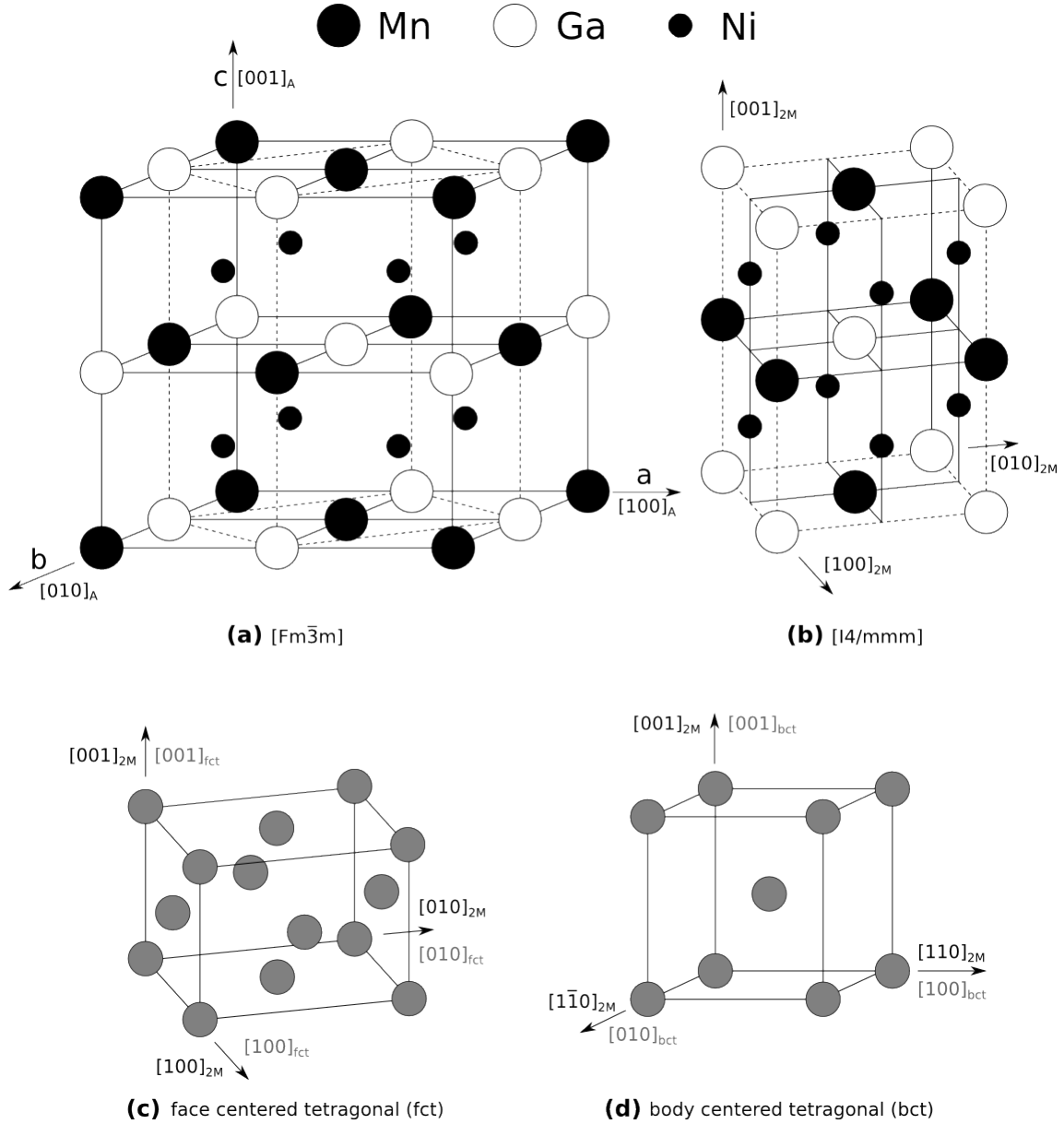
Figure II.3: **(a)** The Heusler $L2_1$ structure of Ni_2MnGa with the unit cell of the 2M unmodulated tetragonal martensite seen in (b) indicated by the broken lines.
(b) The unit cell of the 2M unmodulated tetragonal martensite.
(c) The face centered tetragonal (fct) cell, half of (b).
(d) The body centered tetragonal (bct) cell, one quarter of (b).
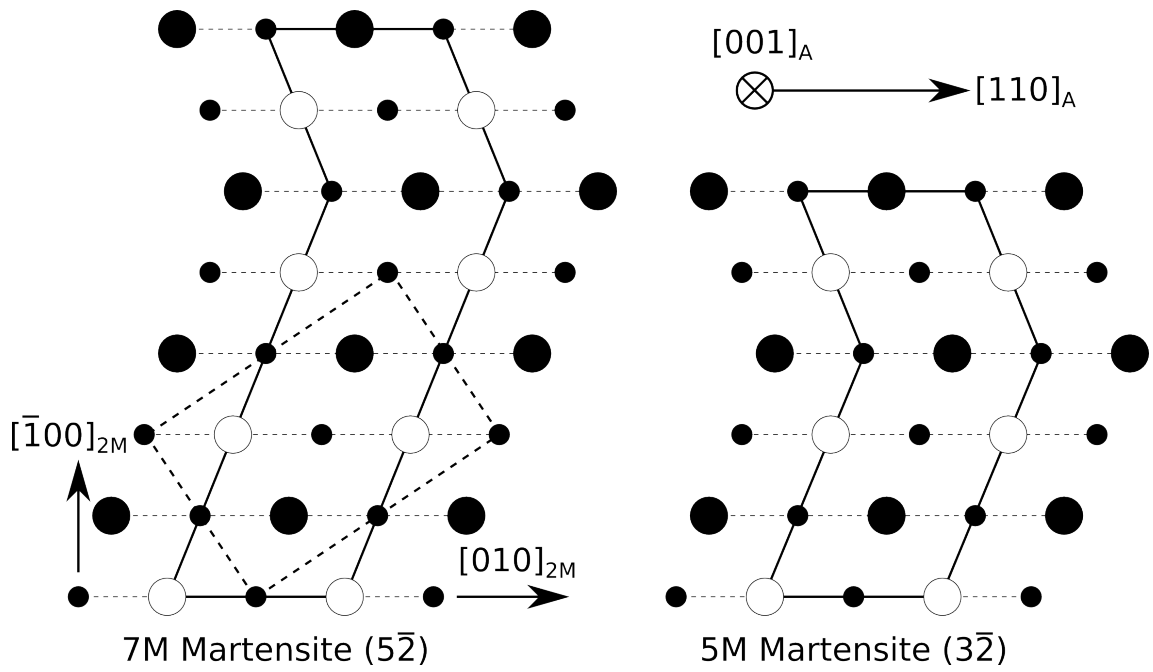For the lenghts of the base vectors of the corresponding unit cells refer to Table II.1.

Figure II.4: Schematic of 7M and 5M martensitic structures. The projections of the $(200)_{2M}$ planes are shown.

Chapter III

Experimental Procedures

During the course of this work several methods of preparation and analysis were used, all of which are described in the following sections.

The starting material was provided by Prof. Peter Müllner of the Boise State University, ID, USA. It was coarse grained and had the stoichiometric composition of $Ni_{54}Mn_{25}Ga_{21}$ - or in alternative nomenclature $Ni_{2.16}MnGa_{0.84}$ - and came in rods with 8 mm in diameter (see also section III.1). Discs with thicknesses between 0.4 and 0.5 mm were cut from the rod via spark erosion and subsequently subjected to severe plastic deformation (SPD) via high pressure torsion (HPT) to procure significant grain refinement. The applied pressure of 8 GPa and polishing reduced the thickness in the order of about 20 %. To gain TEM samples, smaller discs with a diameter of 2.3 mm were stamped out of the deformed disc via spark erosion (see Figure III.1). Via the following equation the degree of deformation can be calculated:

$$\gamma = \frac{n \cdot 2\pi \cdot r}{d} \tag{III.1}$$

γ_{max} is the degree at $r = 4$ mm (at the HPT disc's edge) and γ_{eff} the effective degree at the center of the smaller TEM discs ($r = 2.85$ mm), where the actual TEM analysis was conducted (see Figure III.1). The degree can be given in percent via $\gamma \cdot 100$.

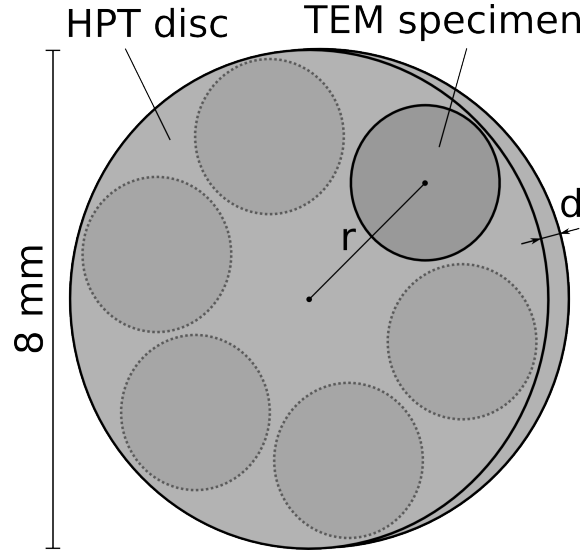| n	d	$\gamma_{\max}$	γ_{eff}
50 turns	0.4 mm	$3.1 \cdot 10^5$ %	$2.2 \cdot 10^5$ %
100 turns	0.3 mm	$8.4 \cdot 10^5$ %	$6.0 \cdot 10^5$ %

Table III.1: Degree of deformation.

Figure III.1: HPT discs were cut via spark erosion from a rod with a diameter of 8 mm. The thickness d of the resulting discs varied between 0.4 to 0.5 mm. To obtain TEM samples, smaller discs were stamped via spark erosion. Radius r and thickness d are important for the determination of the degree of deformation (see Equation III.1 and Table III.1).

The final steps of sample preparation for TEM analysis consisted of dimpling the stamped discs to a thickness of 20 to 30 μm at their center followed by ion milling until a hole with thin edges transparent to the electron beam was formed.

Those 50 and 100 turns HPT discs were subjected to heat treatment to obtain a well ordered Heusler structure. Heat treatment was conducted via Differential Scanning Calorimeter (DSC) under flow of Ar protective gas. The use of a DSC not only allowed controlled heat treatment itself (which could have been done with a simple oven), but also the observation of heat flux arising by dynamical irreversible processes associated with chemical reordering and phase transitions.

X-ray experiments were conducted for structural analysis in addition to that via TEM SAD. Finally, TEM investigation was conducted to determine grain size, lattice structure and lattice constants. The special method of lattice fringe imaging was used to determine the 7M martensitic structure.

III.1 $\mathbf{Ni_{54}Mn_{25}Ga_{21}}$

The Ni-Mn-Ga alloy was provided by Prof. Peter Müllner at Boise State University, ID, USA. It was vacuum-induction melted. The elements had a purity of 99.9% for Ni, 99.95% for Mn, and 99.999% for Ga (all metal basis) and were cast into a copper mold. The nominal composition was 54.0±0.4, 25.0±0.2 and 21±0.2 at.-% of Ni, Mn and Ga, respectively. The error was determined from weight loss after casting. Subsequently the alloys were sealed in quartz tubes under vacuum and were homogenized at 1073 K for 100 h followed by quenching into water[21]. The specific stoichiometric alloy analyzed in this work is a high temperature (ferromagnetic) shape memory alloy with a ausenite start temperature A_S of about 200 °C. It was chosen because the martensitic transformation occurs at high temperature. Electronic properties - that is: especially the ratio of conduction electrons e over the lattice parameter a - is vital for phase stability[1, 22, 23]. Also the Curie temperature is dependent on the alloy concentration.

III.2   Methods of Preparation

III.2.1   Spark Erosion

Spark erosion, or more commonly known as electric discharge machining (EDM), is a technique where materials are cut not by mechanical forces but by applying voltage to the electrically conductive specimen and the tool so that at minimal distance sparks occuring between the two remove material both from the specimen and the tool[11]. This technique was used for stamping (as shown in Fig. III.2) as well as cutting, where the tool was a moving wire.

III.2.2   High Pressure Torsion

High pressure torsion (HPT) means that a specimen is put between two plungers where one rotates along its middle axis. It is considered to be a technique applicable to reach strong grain refinement through severe plastic deformation (SPD) of Ni-
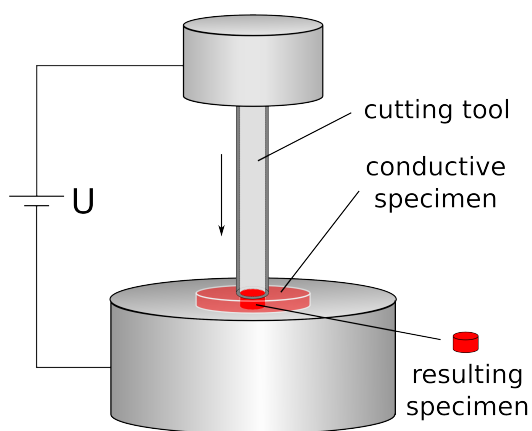
Figure III.2: Spark erosion. Voltage is applied to the cutting tool and specimen, thus both being eroded due to sparkovers.

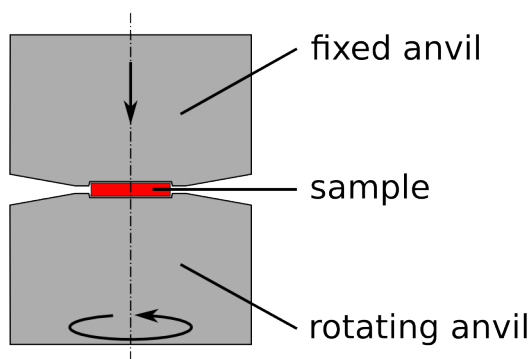Mn-Ga alloys[24]. In the line of this work the applied pressure was 8 GPa and the number of rotations were 50 and 100.

Figure III.3: High pressure torsion. The upper anvil exerts pressere while the lower one rotates around its axis.

III.2.3   Dimpling

Dimpling is a technique where indentations are made on both sides of the desired TEM sample. This is accomplished by rotating the sampe around its center axis and grinding with an orthoganally rotating disc on both sides one after the other[11] (see Figure III.4). When a thickness of about 20 to 30 μm is reached, further thinning of the sample can be done by ion milling.
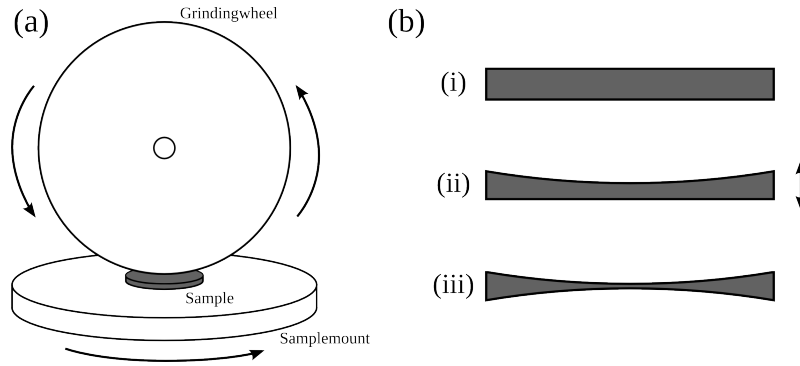
Figure III.4: **(a)** Schematic of a dimpler. The two discs rotate normal to each other, the upper one grinding into the specimen. **(b)** The dimpling process. (i) Ungrinded specimen is put into the dimpler, (ii) so it can be indented on one side after which (iii) it's turned around to indent onto the other side. (by courtesy of Peter Schindler[25])

III.2.4   Ion Milling

Ion beam etching - or simply ion milling - uses a focused beam of ions (mostly positively charged Ar-ions) accelerated with high voltages causing a samples' surface to erode. In the line of this work a *Bal-Tec RES-101 Ion Mill* was used which has Ar-ion source between 1 -10 kV, up to a 200 mA current and the FWHM between 0.8 and 2.5 mm[26]. For a detailed schematic see Figure III.5.
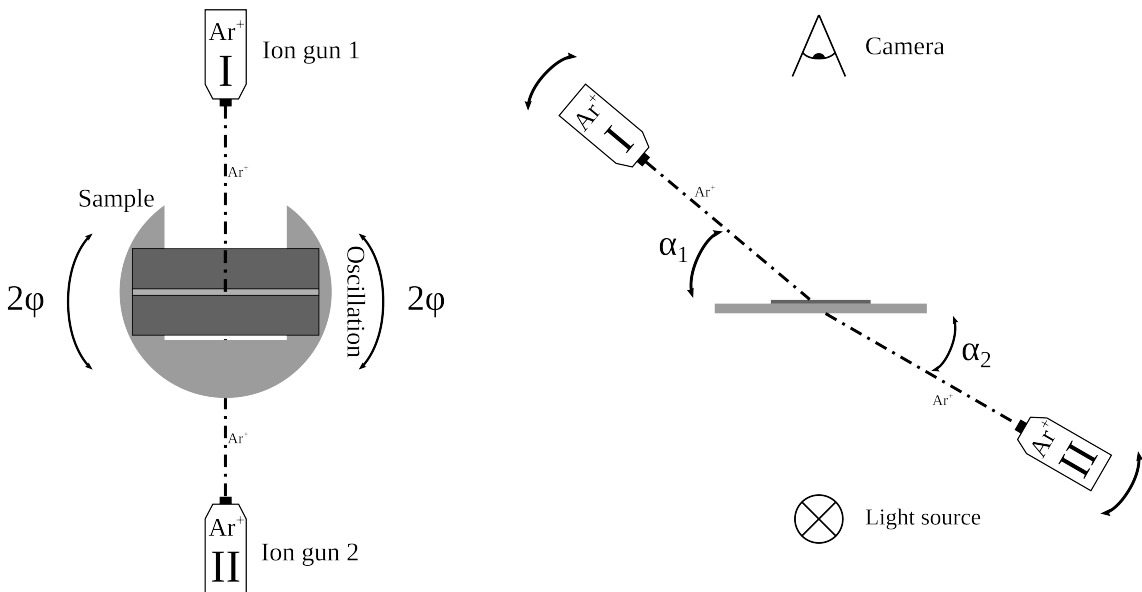

Figure III.5: Schematic of a *Bal-Tec RES-101* ion mill. **Left** Top view. **Right** Side view. (by courtesy of Peter Schindler[25])

III.3   Methods of Analysis

Both for TEM and XRD the *jems* software by P. Stadelmann (EPF Lausanne, Switzerland) was used to calculate the positions of the lattice reflections of the 2M, fcc, bcc and 7M structures. The calculated positions of the reflections were compared with those obtained by the experiment to identify the corresponding lattice structures. It should be noted that in the calculations the lattice parameters were taken from literature (see Table V.1) and were not optimized to perfectly fit the experimental results (i.e. this might cause some deviations of the experimental and calculated positions of the reflections).

III.3.1   Differential Scanning Calorimetry

Differential scanning calorimetry (DSC) is a technique where the difference in the amount of heat required to increase the temperature of a sample and reference is measured as a function of temperature (see Figure III.6). It is primarily used to detect phase transformations, where melting as an endothermic process would render an endothermic signal since the specimen will absorb more heat than to the reference. Similarly a crystallization process will render an exothermic signal since the specimen will show less heat absorbance than the reference[27]. In the line of this work two DSC's were used, both with a constant heating/cooling rate of 20K/minute: a *Perkin Elmer DSC 7* (power compensated, see Figure III.7) as well as a *Netzsch DSC 204* (heat flux).

The analyses of the DSC cycles were done via the software *Netzsch Proteus Analysis*. The tangent method was used to determine the temperature values.

III.3.2   X-Ray Powder Diffraction

X-ray powder diffraction is a technique for determination of crystal sturucture and/or chemical composition of a given sample. Via the Bragg equation

$$2d \sin \Theta = n\lambda \qquad\qquad\qquad \text{(III.2)}$$
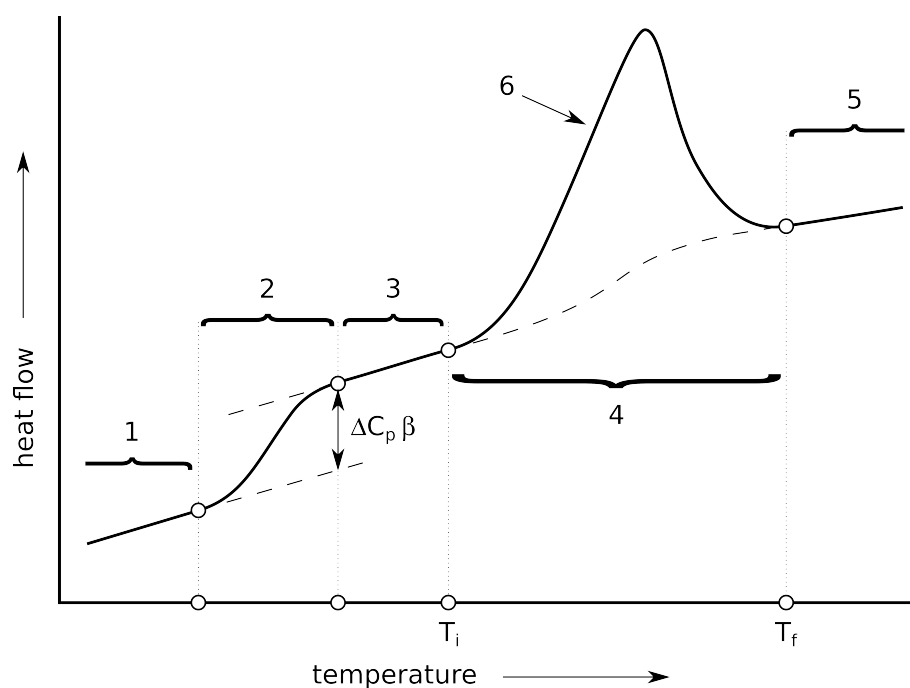
Figure III.6: How to read a DSC-curve. Adapted from [27].
ΔC_p change of heat capacity; T_i, T_f initial/final peak temperature.
1 initial segment, **2** step due to ΔC_p **3** measured curve, **4** interpolated base line, **5** final segment, **6** peak (endothermic, 1$^{\text{st}}$ order transition).
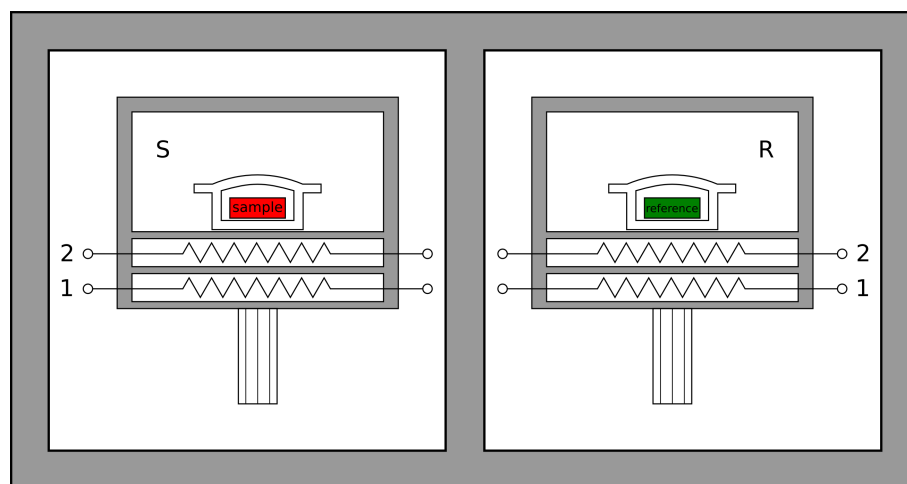

Figure III.7: Schematic of a power compensated DSC. **1** heating wire, **2** resistance thermometer. Adapted from Ref. [27], Fig. 2.4.

structures such as atomic lattices in a crytalline material can be determined by the result of a diffraction experiment (see Ref. [11], Ch. 3.10.B.) (d... lattice plane distance; Θ... diffraction angle; λ... wavelength; n... integer number). In the case that the path difference is a multiple of $\lambda/2$, constructive interference occurs.
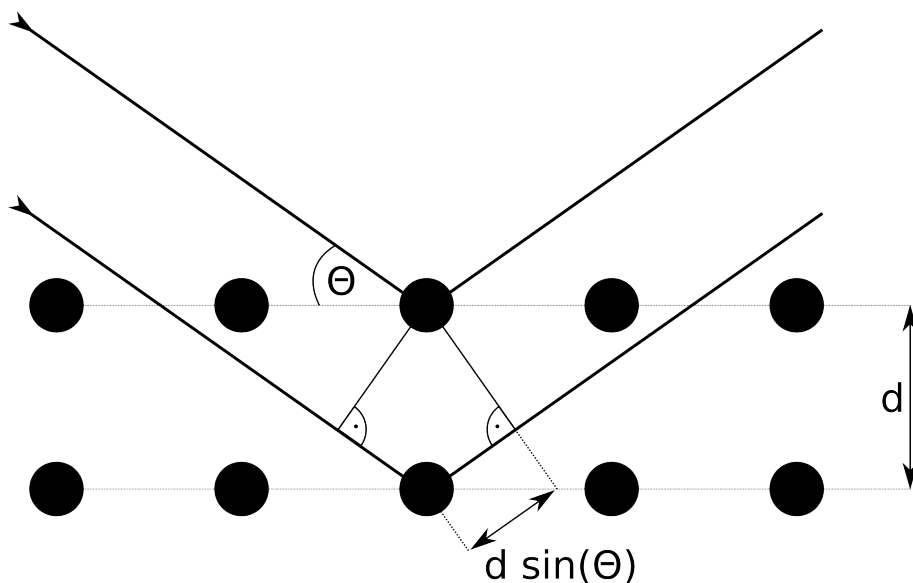
Figure III.8: Illustration of a Bragg reflection in a crystalline material.

During the course of this work a *Bruker D8* as well as a *PANalytical X'PRO* powder diffractometer were used. In both cases Cu Kα emission was used.

III.3.3   Transmission Electron Microscopy

TEM is a poweful tool in material science and other fields. It allows for the observation of structures from several hundreds of micrometres down to about 50 picometres using state of the art abberation corrected electron microscopes. I the line of this work a *Philips CM200 TEM* with a maximum acceleration voltage of 200 kV ($\lambda = 2.5097$ pm) was used. There were several techniques used for all of which a short introduction follows: bright and dark field imaging, selected area diffraction as well lattice fringe imaging.

Imaging and Diffraction

There are two basic imaging techniques of a TEM: bright field (BF) and dark field (DF). In bright field imaging (fig III.9, left) only the central and thus undiffracted beam of electrons is allowed to pass the objective aperture. A dark field image is obtained by selecting scattered electrons of any form. Usually, when doing dark field

imaging the incident beam is tilted, so that the scattered beam remains on axis, this is called centered dark field[11].

When inserting a selector aperture between objective aperture (where the 1st diffraction pattern (DP) is formed) and the intermediate lens (the latter being used with lower voltage than in imaging mode) this is called selected area diffraction or short SAD (fig III.9, right).
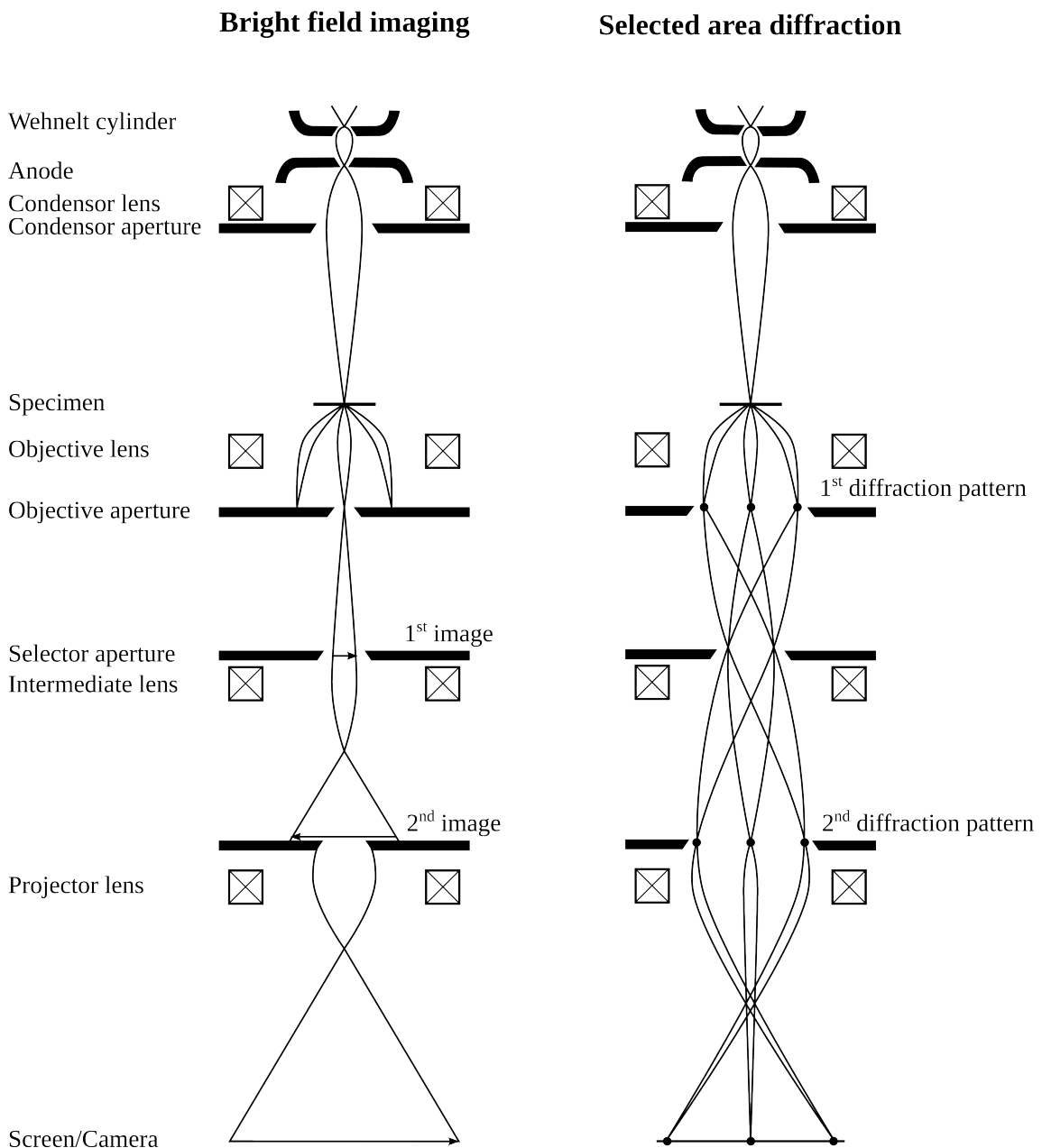
Bright field imaging   **Selected area diffraction**

Wehnelt cylinder

Anode
Condensor lens
Condensor aperture

Specimen

Objective lens

Objective aperture   1st diffraction pattern

1st image

Selector aperture
Intermediate lens

2nd image   2nd diffraction pattern

Projector lens

Screen/Camera

Figure III.9: Schematic of a TEM (by courtesy of Peter Schindler[25]).

Table III.2: Notation for lattice fringes

|	
Ψ	*Total* wave function of the electron beam
$\varphi_{\mathbf{a}}$	Amplitude of the *direct* beam
$\varphi_{\mathbf{b}}$	Amplitude of the *diffracted* beam
$\xi_{\mathbf{b}}$	extinction distance (characteristic length for reflection $\mathbf{b}$)
$\mathbf{k}$	Electron wave vector in the specimen
$\mathbf{r}$	Distance from a certain point P at the bottom of the specimen to the scattering center
s	Excitation error (s_{eff} effective excitation error)

Lattice Fringe Imaging
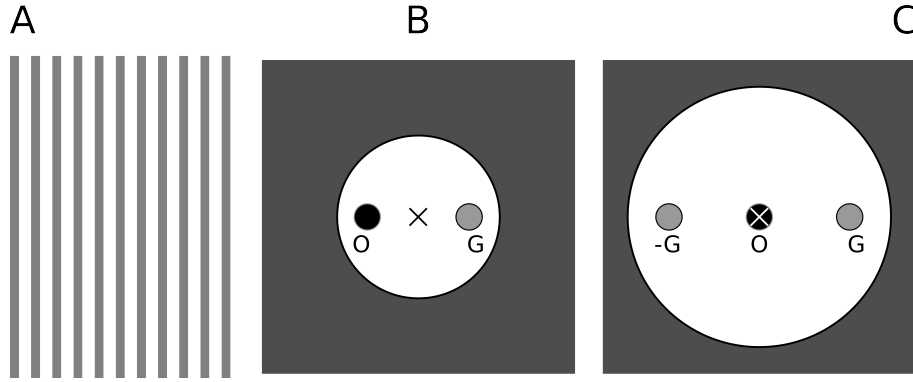
Figure III.10: A. The sinusoidal pattern observed in the bright field when conducting lattice fringe imaging; $\mathbf{g}$ (in text: $\mathbf{b}$) is normal to the fringes. **B.** Usual selection of the direct and one diffracted beam to obtain lattice fringes. **C.** On-axis three-beam geometry. (from [11], Figure 27.1.)

In lattice fringe imaging not only one diffracted beam is selected to pass the objective aperture, like the center beam in bright field imaging or one of the diffracted beams in dark field imaging, but two or more (see Figure III.10).

To understand the appearance of lattice fringes let us assume the two selected beams $\mathbf{a}$ and $\mathbf{b}$ interfere with each other (see Ref. [11], Ch. 27).

$$\Psi = \varphi_{\mathbf{a}}(z)e^{2\pi i\mathbf{k}_I\cdot\mathbf{r}} + \varphi_{\mathbf{b}}(z)e^{2\pi i\mathbf{k}_D\cdot\mathbf{r}} \qquad\qquad \text{(III.3)}$$

where $\mathbf{k}_I$ is the wave vector of the incident wave and $\mathbf{k}_D$ the wave vector of the diffracted wave and $\mathbf{k}_D = \mathbf{k}_I + \mathbf{b} + s_{\mathbf{b}} = \mathbf{k}_I + \mathbf{b}'$.

We substitute $\varphi_{\mathbf{a}}(z) = A$ and $\varphi_{\mathbf{b}}(z) = B \cdot e^{i\delta}$ where $B = \frac{\pi}{\xi_{\mathbf{b}}} \frac{\sin \pi t s_{\mathrm{eff}}}{\pi s_{\mathrm{eff}}}$ and $\delta = \frac{\pi}{2} - \pi t s_{\mathrm{eff}}$. The specimen is very thin, so we can write $s_{\mathrm{eff}} = s$. This means Equation III.3 can be written as

$$\Psi = e^{2\pi i \mathbf{k}_I \cdot \mathbf{r}} \cdot \left(A + B e^{i(2\pi \mathbf{b}' \cdot \mathbf{r} + \delta)} \right) \tag{III.4}$$

Intensity can now be written as

$$\begin{aligned} I &= A^2 + B^2 + AB \left(e^{i(2\pi \mathbf{b}' \cdot \mathbf{r} + \delta)} + e^{-i(2\pi \mathbf{b}' \cdot \mathbf{r} + \delta)} \right) \\ &= A^2 + B^2 + 2AB \cos(2\pi \mathbf{b}' \cdot \mathbf{r} + \delta) \end{aligned}$$

$\mathbf{b}'$ is orthogonal to the beam (parallel to x). Taking the definition of δ from above, the intensity distribution in the bright field image is

$$I = A^2 + B^2 + 2AB \sin(2\pi \mathbf{b}' x - \pi s t) \tag{III.5}$$

It can be seen that the intensity is a sunusoidal oscillation orthogonal to $\mathbf{b}'$, with a periodicity depending on excitation error s and time t. These fringes can be related to the distance of the lattice planes orhogonal to $\mathbf{b}'$[11].

Chapter IV

Experimental Results

During the course of this work, both a 50 HPT-turns specimen and a 100 HPT-turns specimen were analyzed before and after heat treatment, the results of which were consistent with each other. The sample choice in the following sections is based upon quality and informative value of the respective images.

The lattice parameters were all calculated from the analysis of TEM SAD images. The range of the error is similar for all calculated lattice parameters and constitutes to about 10%. This is due to a systematical error of about 5% coming from a lack of accurate reproducibility of calibration e.g. by the remanescence of magnetic lenses. Another 5% are from the stochastic error, e.g. the accuracy of identifying the exact positions of the Bragg reflection peaks in the TEM SAD images.

All analyses in the TEM and the XRD were conducted at room temperature.

IV.1 TEM analysis

IV.1.1 Coarse Grained

In the coarse grained material - that is: before HPT deformation - we can see that each martensitic variant is internally twinned (Figure IV.1). The diffraction pattern (Figure IV.2) indicates a 2M tetragonal I4/mmm structure of the martensite. The lattice parameters were calculated as $a = b = 0.82$ nm and $c = 0.69$ nm ($c/a = 0.84$). The grain size is in the range of several hundreds of microns[28].
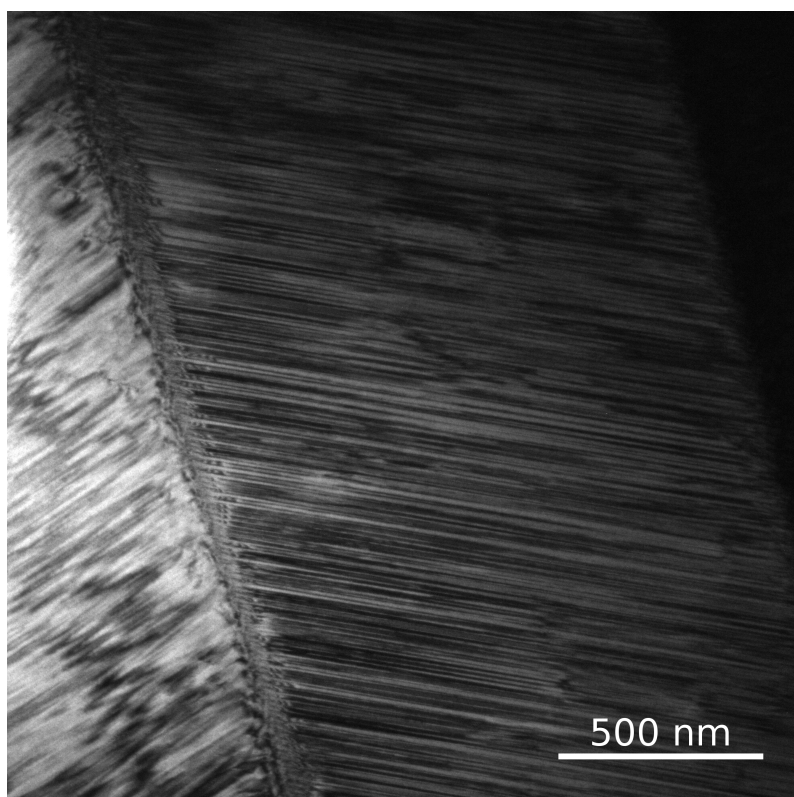
Figure IV.1: Bright field image of $Ni_{54}Mn_{25}Ga_{21}$ prior to HPT.
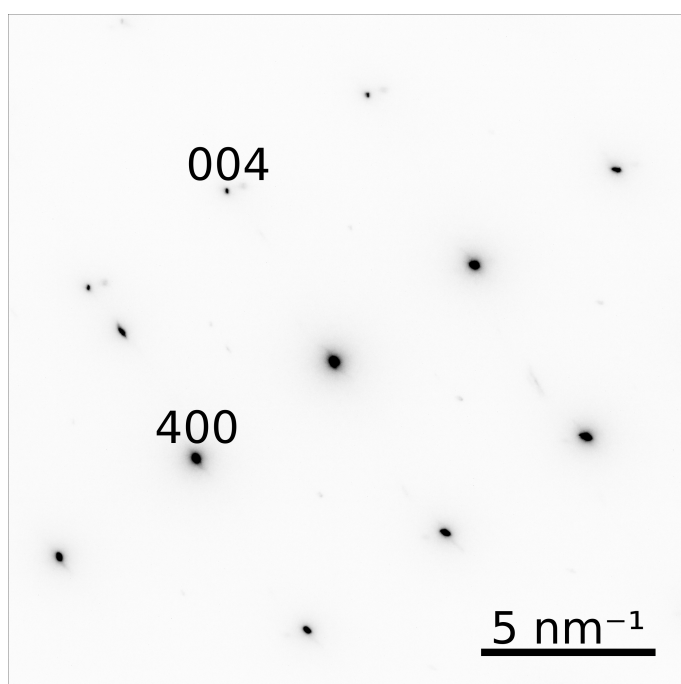

Figure IV.2: Diffraction pattern prior to HPT showing 2M tetragonal martensite.

IV.1.2 HPT deformed without heat treatment

After HPT deformation structural disordering was observed. At room temperature a face centered tetragonal (fct) phase (disordered 2M martensite) as well as a disordered fcc phase (γ-phase) were observed (Figure IV.5). It should be noted that superstructure reflections characterisic for the chemical order of the 2M martensite were not observed. The degree of order was determined indirectly through different observations as specified in the Discussion (Chapter V). The fct cell is to be undestood according to the nomenclature of Tian et al.[29], where the lattice is double the size of the actual fct lattice in the [001] direction (see Figure II.3 & Table II.1). The lattice parameters of the disordered fct were calculated as $a = b = 0.73$ nm and $c = 0.63$ nm ($c/a = 0.86$ nm). The lattice paramter for the γ-phase is $a = 0.35$ nm. In the bright and dark field images (Figures IV.3 & IV.4) complex contrast patterns are observed due to lattice strains and Moiré patterns caused by different crystalline orientations or lattice structures overlapping in the TEM projection. The grains seem to be strongly fragmented by the formation of subgrain boundaries. However, due to the complex contrast, the subgrain boundaries are hardly visible. Neglecting the Moiré patterns, in the TEM dark field images large patches of bright and rather uniform average contrast are frequently observed (see A in Figure IV.4). These large fragments have a size in the range of several hundreds of nanometres. In addition, contrast variations on a smaller scale were observed (see B in Figure IV.4). Most of these fragments have an average size of about 120 ± 6 nm.
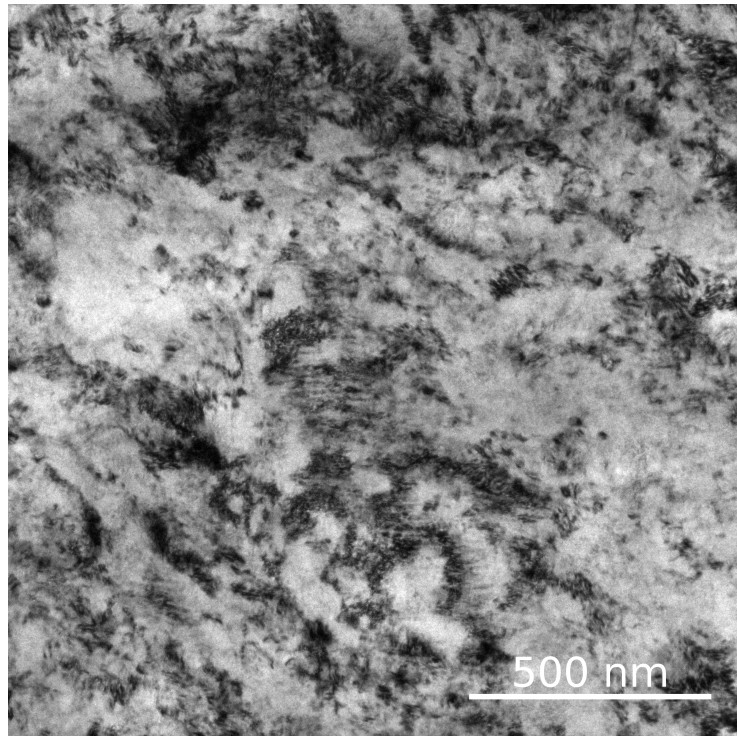
Figure IV.3: Bright field image, HPT 50 turns, no heat treatment. Strong grain fragmentation can be observed due to severe plastic deformation.
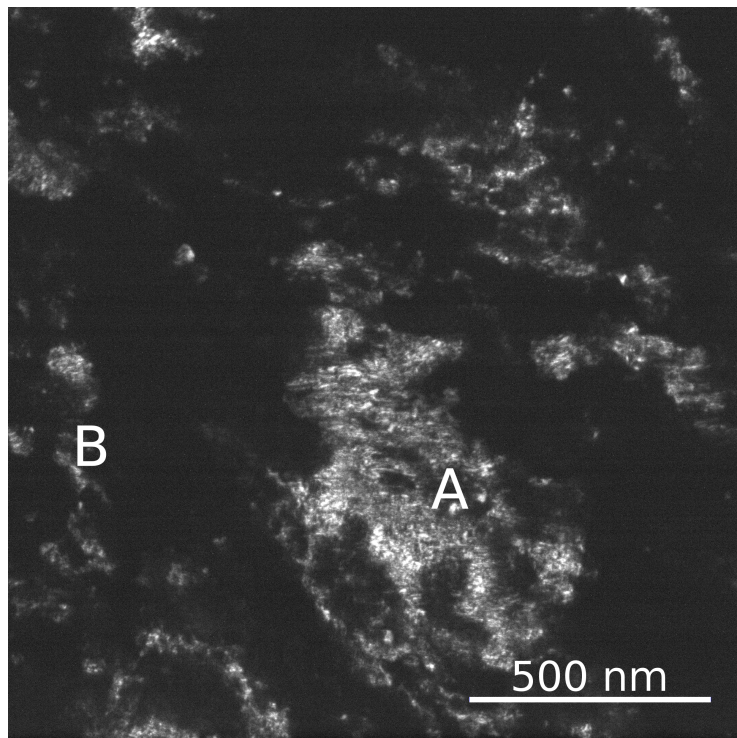

Figure IV.4: Dark field image. HPT 50 turns, no heat treatment. **A.** Large areas of uniform contrast, size in the range of hundreds of μm. **B.** Small contrast variations, average size in the range of 120 ± 6 nm.
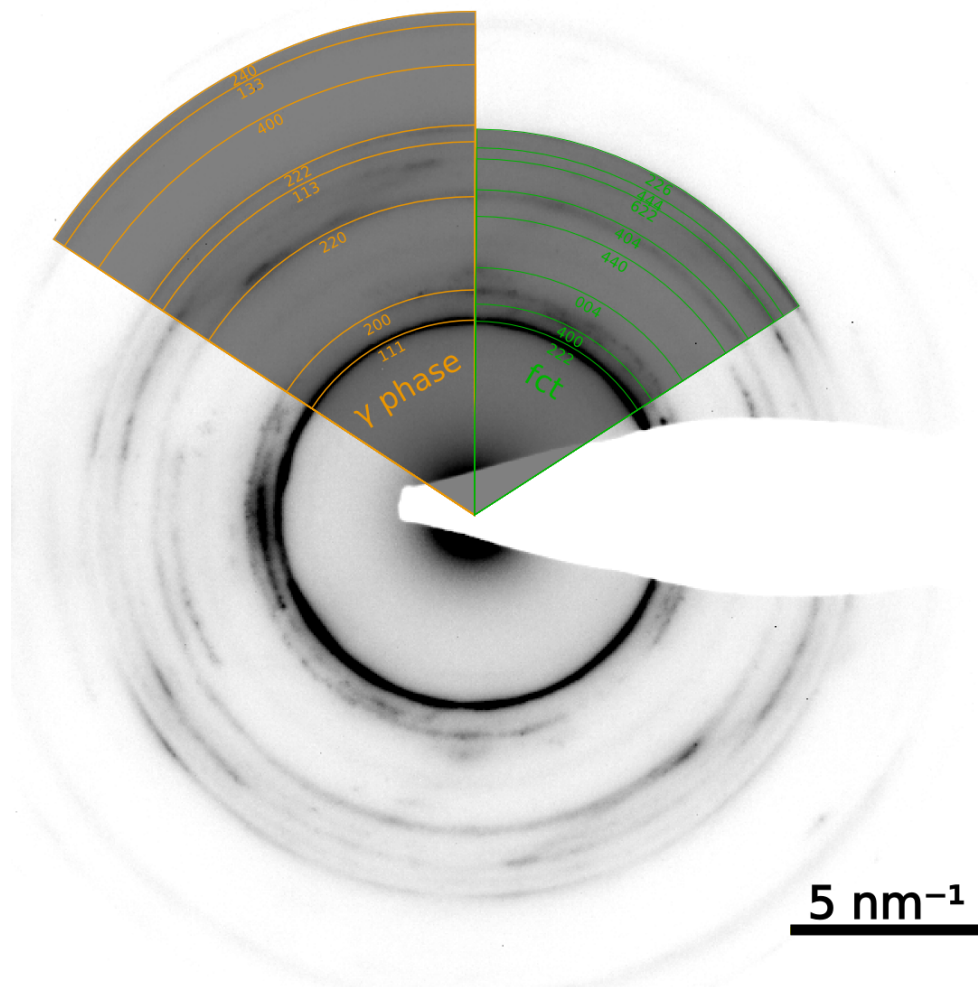
Figure IV.5: Selected area diffraction image, HPT 100 turns, no heat treatment. Disordered fct and γ-phase is observed.

IV.1.3 420 °C heat treated

Even after isochronal heat treatment to a temperature of 420 °C a rather complex contrast pattern is observed in both the bright and the dark field images (see Figures IV.6 & IV.7). However, as compared to the bright and dark field images of the alloy subjected to HPT without heat treatment (Figures IV.3 & IV.4 also some small grains with a well defined polygonal morphology were observed. These small grains seem to be rather free of dislocations. However there are also patches of complex contrast encountered including such that arise by Moiré effects (Figure IV.6) which are similar to the Moiré effects arising by grain fragments observed in Figure IV.3. Based on SAD taken at various areas of the specimen, most the reflections agree with

a body centered cubic (bcc) phase with a calculated lattice parameter of $a = 0.28$ nm. Almost no intensity arose from fct/fcc (Figures IV.6, IV.7), IV.8).
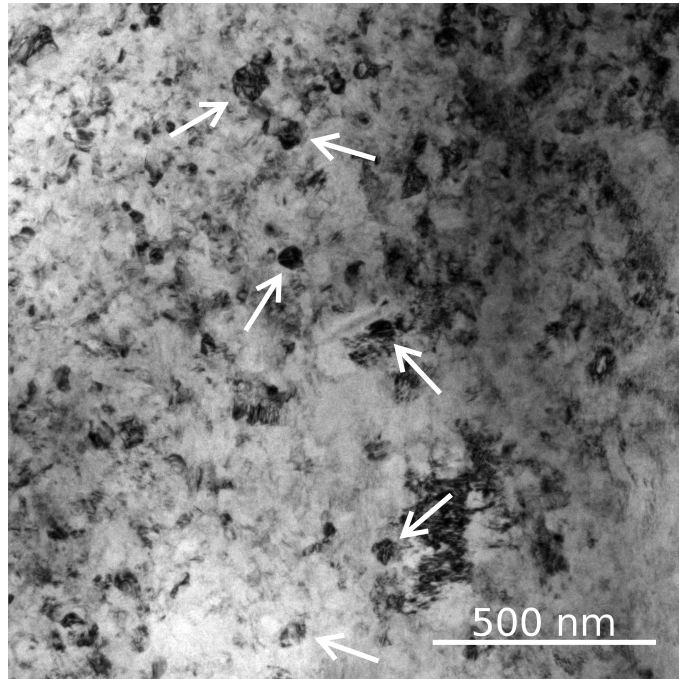

Figure IV.6: Bright field image, HPT 50 turns, heat treatment to a temperature of 420 °C. Arrows indicate small polygonized grains.
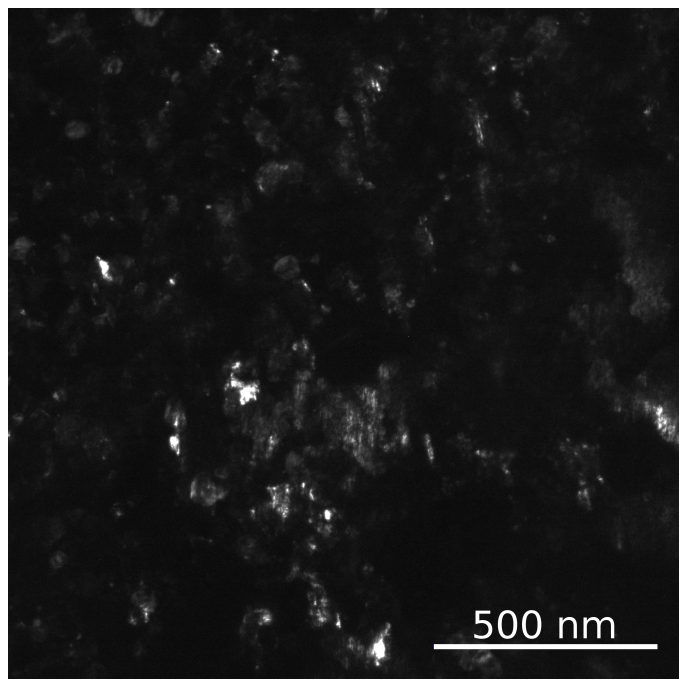

Figure IV.7: Dark field image, HPT 50 turns, heat treatment to a temperature of 420 °C.
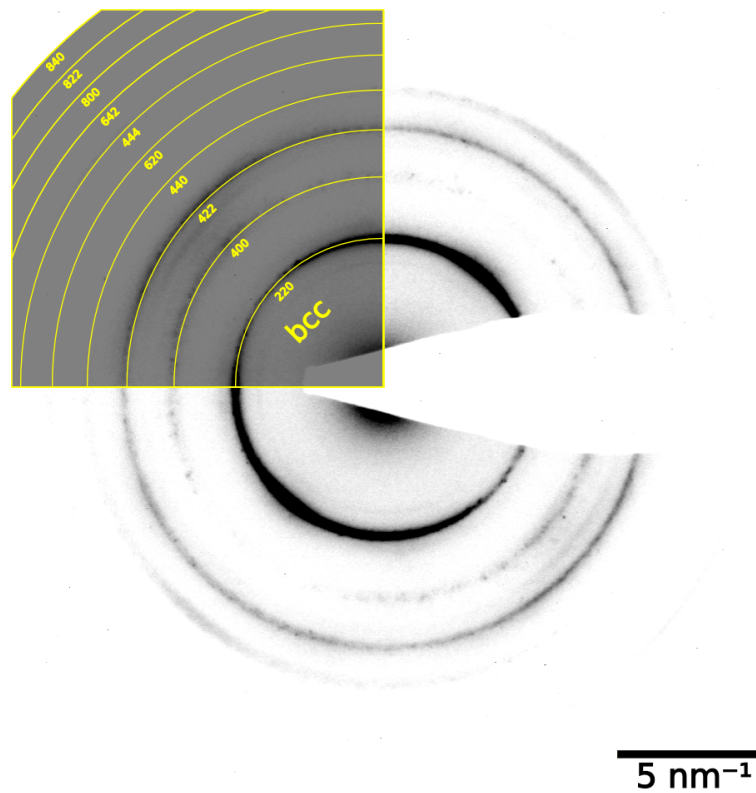
5 nm⁻¹

Figure IV.8: Selected area diffraction, HPT 50 turns, heat treatment to a temperature of 420 °C. Body centered cubic is observed to be the predominant phase due to disorder-caused supression of martensitic transformation.

IV.1.4   500 °C heat treated

After isochronal heating up a temperature of 500 °C, the SAD pattern analysis shows a 7M martensitic structure (Figures IV.9 & IV.13). The dashed lines in Figure IV.9 indicate reflexes of low intensity (according to theorical simulations). Specifically the reflections [2 12 0], [3 8 0] and [0 14 4] of 7M martensite are supposed to be very low in intensity, but were observed to have a relatively high one.

A well defined polygonized submicrocrystalline structure is formed. The grain boundaries are clearly observed both in TEM bright and dark field images (Figures IV.10 & IV.11). The grains contain almost no dislocations and only some small angle grain boundaries. The grain size was measured to be about 140 ± 6 nm. Some of the grains show Moiré effects that might arise from stacking faults and different martensitic variants that overlap in the TEM projection.

Analyzing a 100 turns sample several grains with intramartensitic variant boundaries

were found. The SAD pattern consistenly shows a 7M structure with overlapping reflections from both martensitic variants (Figures IV.14 & IV.15), different variants indicated as A and C). The enclosed angle of the twins is about $125 \pm 3°$. The intervariant junction plane with direction $[1\ \overline{2}\ \overline{7}]$ of the variants is indicated by the red line in Figure IV.15. It exhibits no strong contrast and is very thin, probably in the single nanometre range.
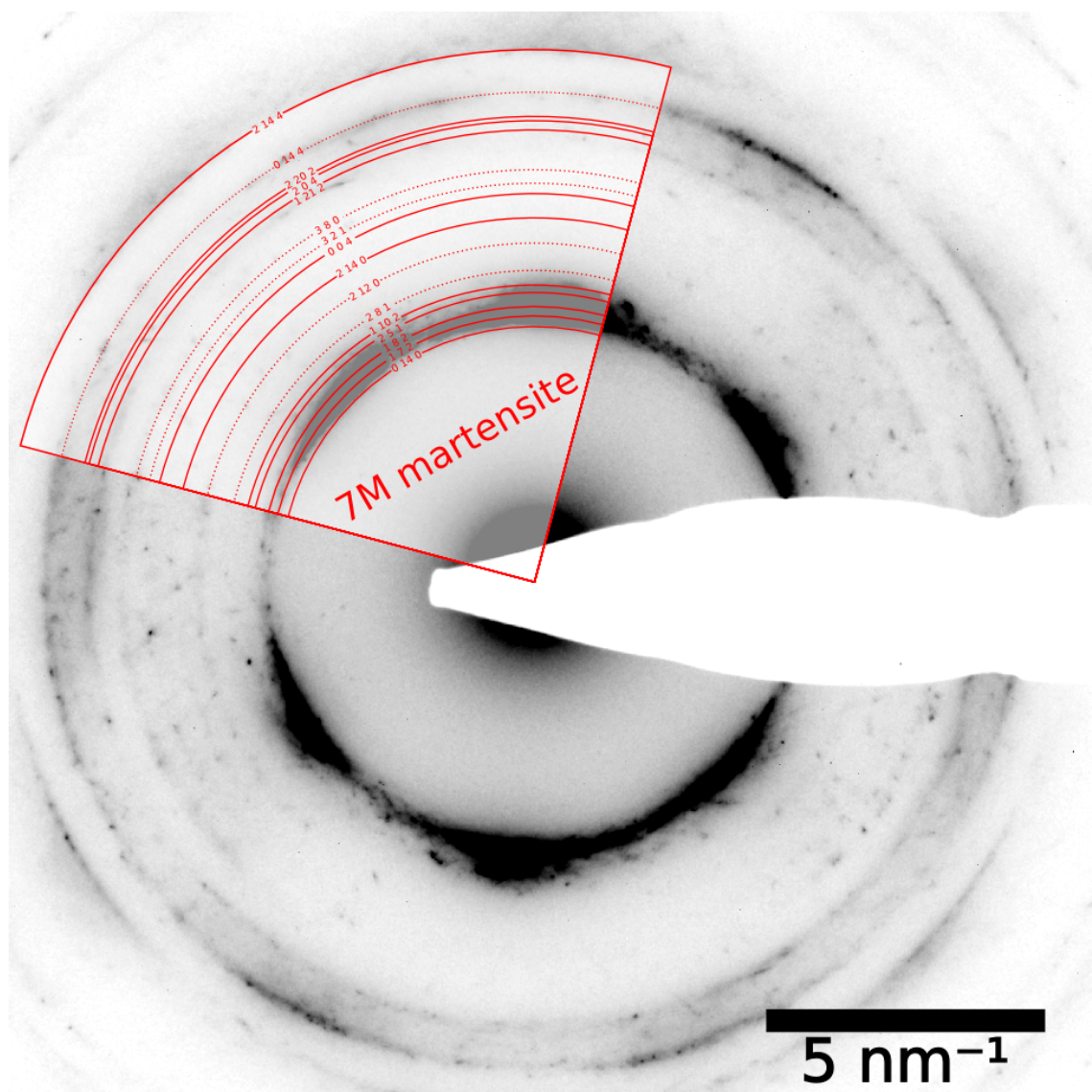

Figure IV.9: Selected area diffraction image, HPT 50 turns, heat treatment to 500 °C. 7M martensite clearly seen to be the predominant phase (confirmed by Figure IV.13 & IV.14).
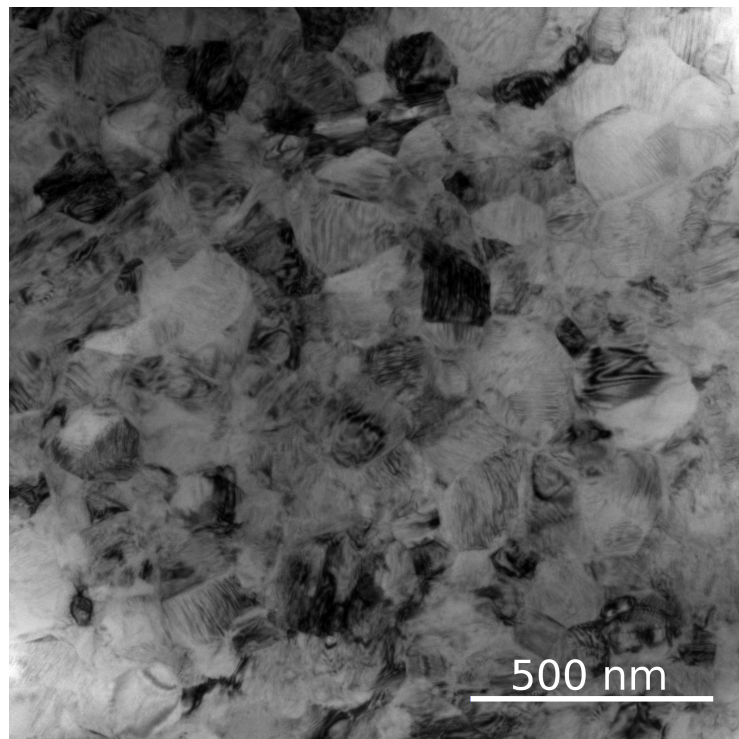
Figure IV.10: Bright field image, HPT 100 turns, heat treatment to a temperature of 500°C. Grain size ca. 140 ± 6 nm in diameter. Twinning and stacking faults render Moiré effects.
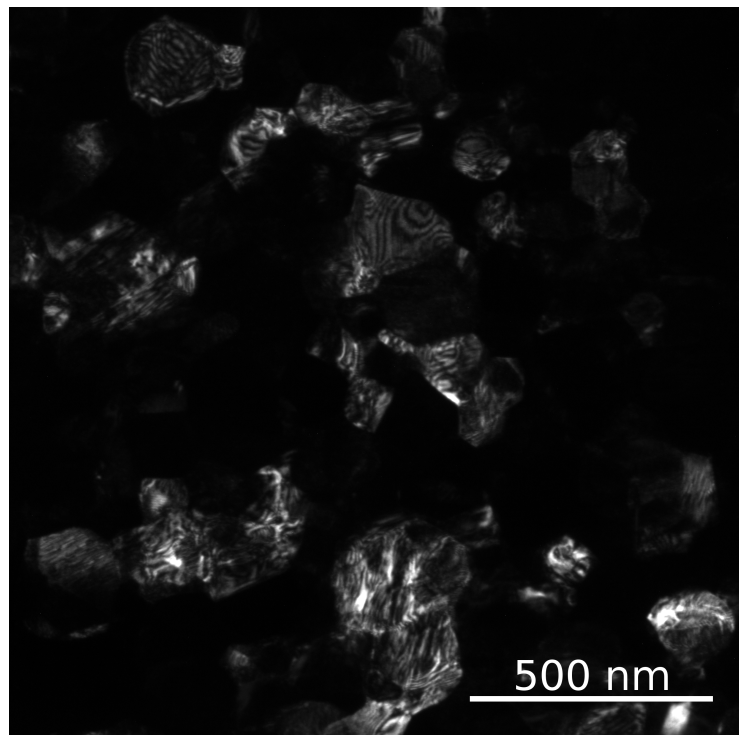

Figure IV.11: Dark field image, HPT 50 turns, heat treatment to a temperature of 500°C.

Analysis of a lattice fringe bright field image (Figure IV.12) showed a structural disorder of 7M stacking sequences. To determine the density of planar defects a profile analysis was conducted of lattice fringes in a typical grain (see Figure IV.12). The average density of planar defects was observed to be approximately 0.15 per nanometre.
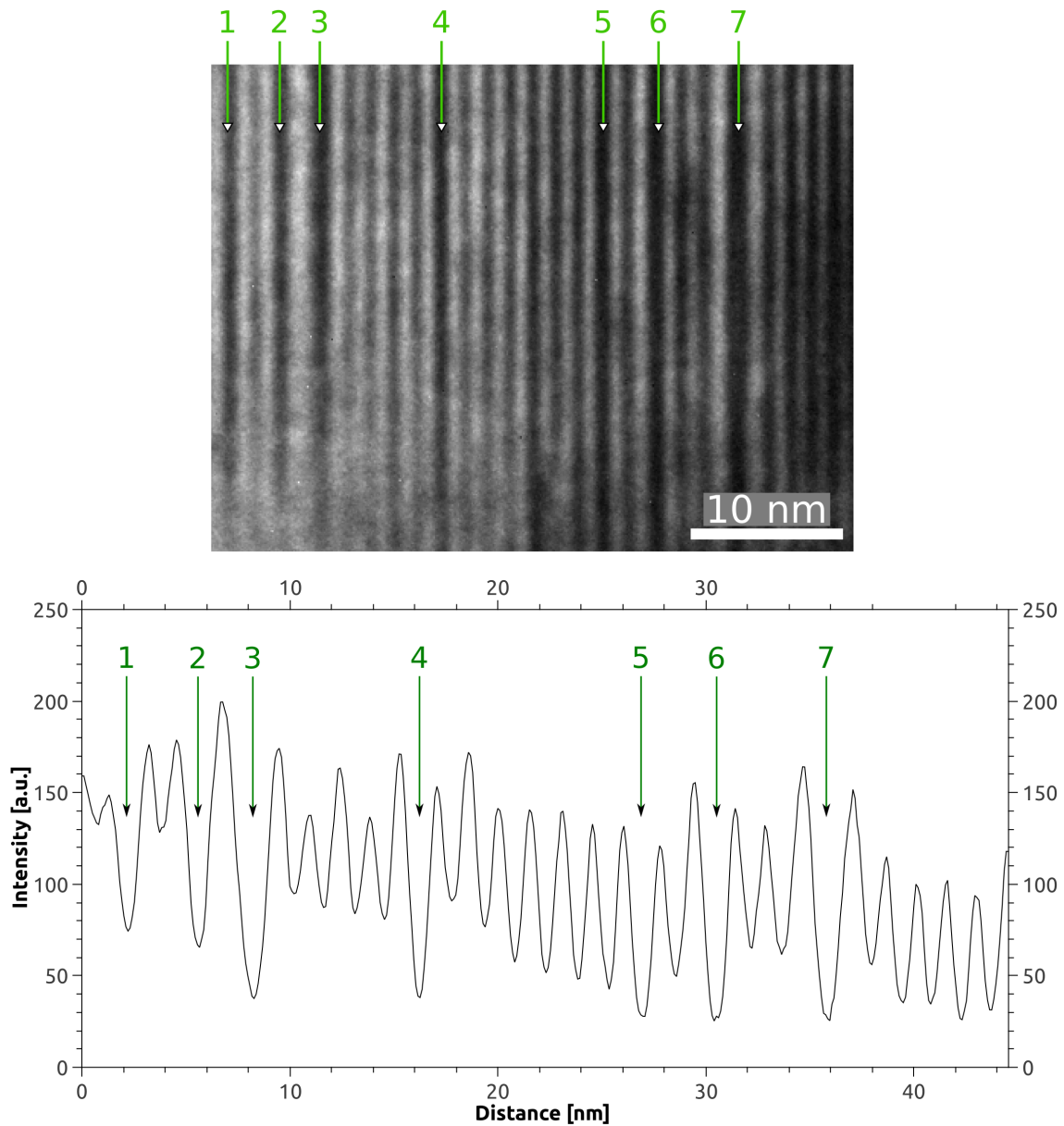

Figure IV.12: Lattice fringes of 7M martensite and corresponding profile analysis. Obtained by allowing [002] and [00$\bar{2}$] reflections to pass the objective aperture. (BF image, HPT 50 turns, heat treatment to a temperature of 500 °C)
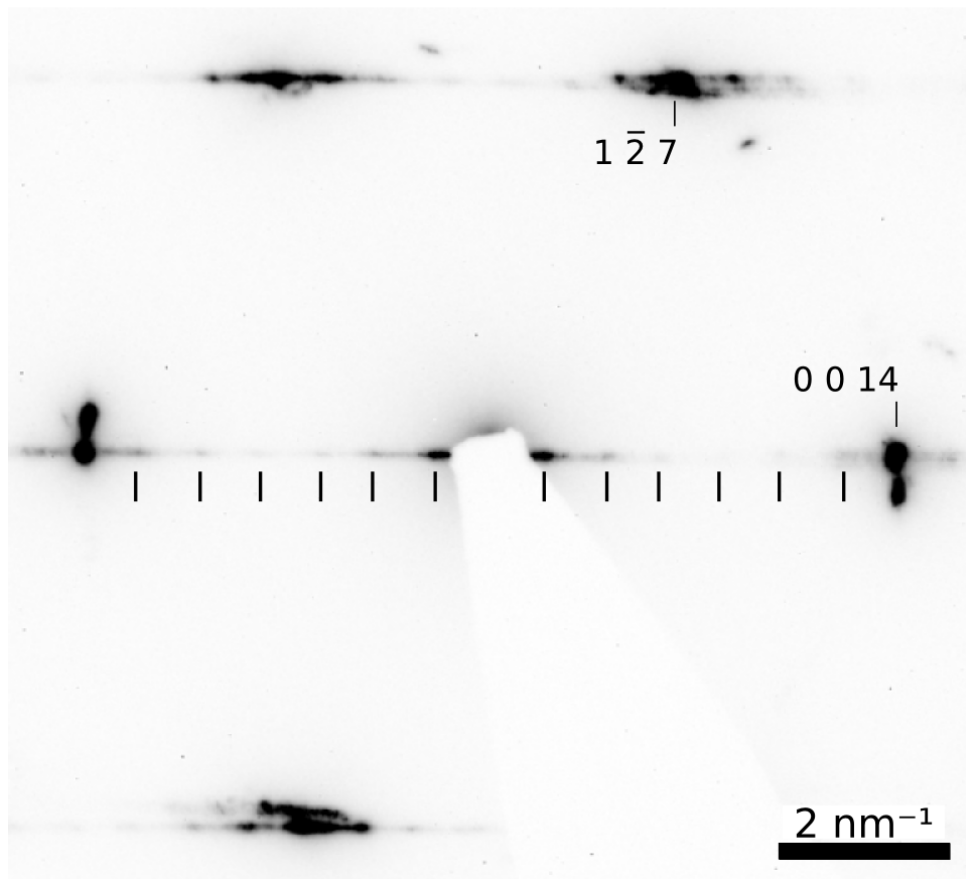
Figure IV.13: Selected area diffraction image, HPT 50 turns, heat treatment to a temperature of 500°C. Reciprocal lattice streaks with sattelite reflections corresponding to 7M martensite indicated by lines can be seen. Beam direction **BD** = [210].
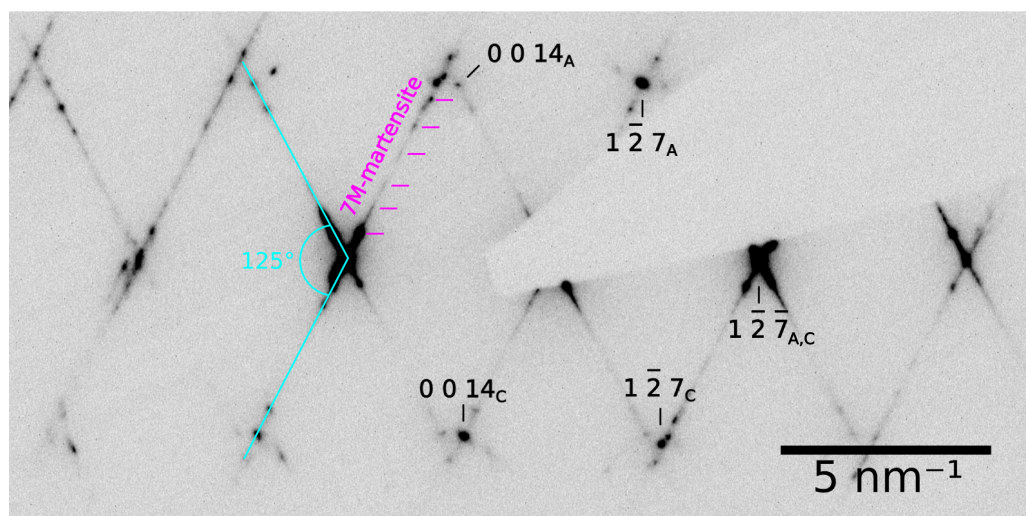

Figure IV.14: Selected area diffraction image, HPT 100 turns, heat treatment to a temperature of 500 °C. Reciprocal lattice streaks with characteristic satellite reflections of 7M martensite - indicated by lines - can be seen. Zone Axis [$\bar{2}\ \bar{1}\ 0$]. Beam direction **BD** = [210]
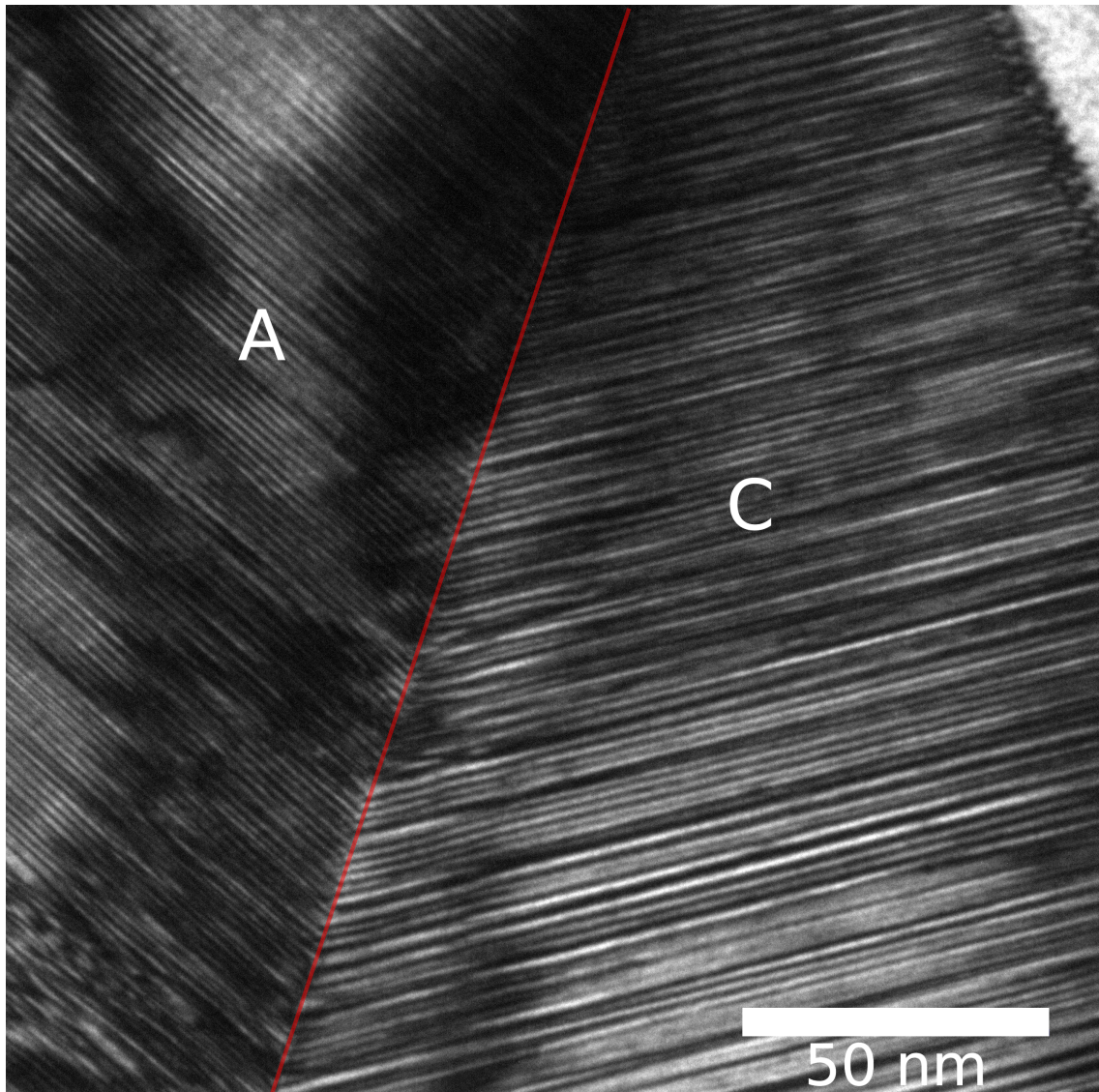
Figure IV.15: Bright field image, HPT 100 turns, heat treatment to a temperature of 500 °C. The intervariant junction plane separating variants A and C of the twins is indicated by the red line. The twins enclose an angle of about $125 \pm 3°$.

IV.2 X-Ray analysis

IV.2.1 Undeformed

Prior to x-ray analysis the sample was heat-treated at a temperature of 800°C for 100 hours, followed by a water quench. Comparison with simulated data showed an good correlation with tetragonal martensite.
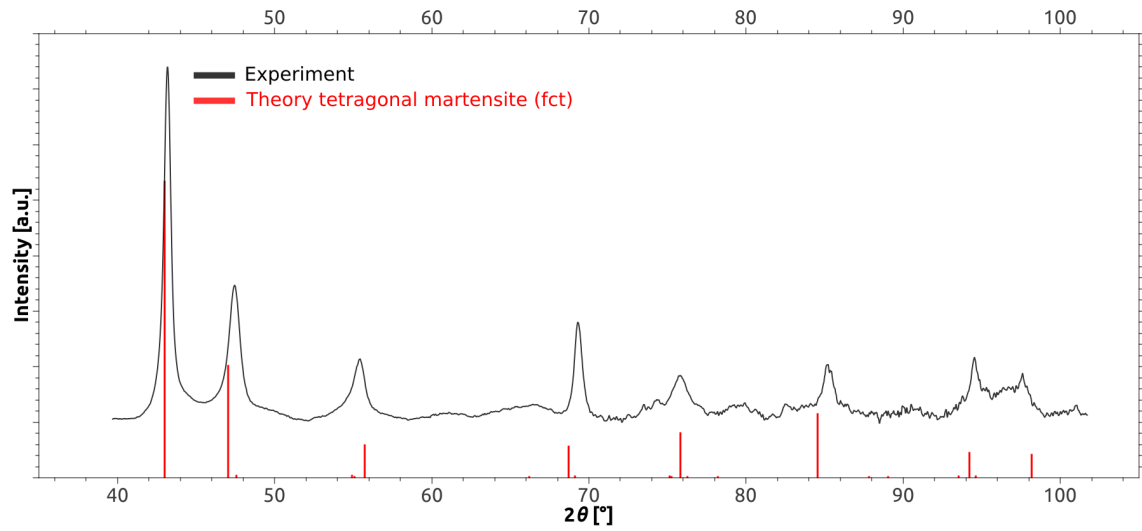
Figure IV.16: Undeformed sample. Singular lines correspond to theoretical calculations. Tetragonal martensite is obseved.

IV.2.2 HPT deformed

Upon deformation x-ray analysis showed predominantly γ-phase with the exception of one peak at $2\Theta \simeq 56°$ which might me caused by a residual from tetragonal martensite.
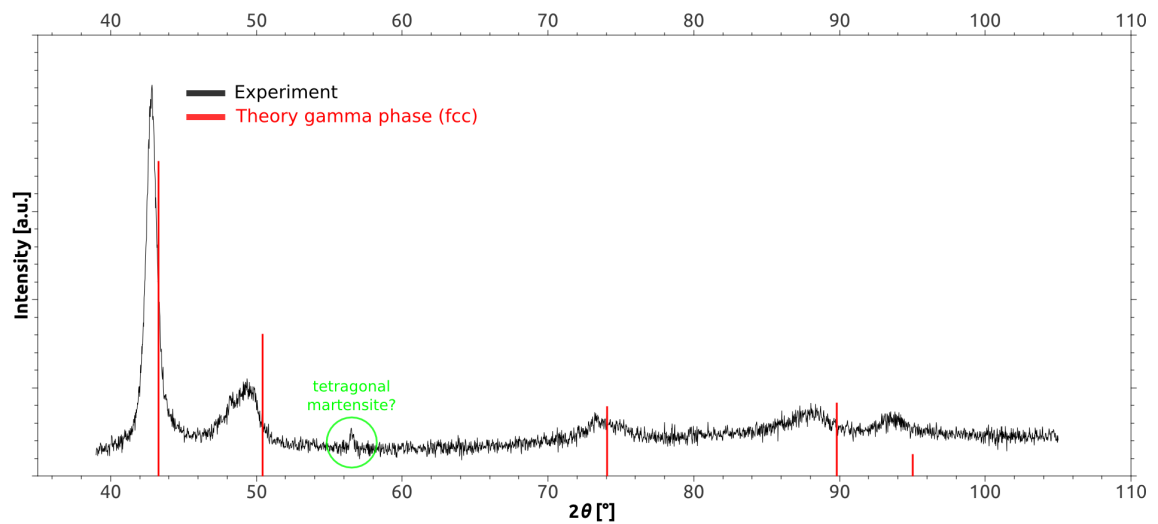
Figure IV.17: HPT deformed without heat treatment (50 HTP-turns). Singular lines correspond to theoretical calculations. Gamma phase (fcc) is observed to be predominant.

IV.2.3   HPT deformed, annealed to 420 °C

Upon heating to 420 °C a clear correlation to body centered cubic phase was detected (Figure IV.18).

Figure IV.18: HPT deformed with heat treatment to a temperature of 420 °C (50 HTP-turns). Singular lines correspond to theoretical calculations. Body centered cubic (bcc) is seen to be predominant.

IV.2.4   HPT deformed, annealed to 500°C

After full heat treatment to a temperature of 500 °C, 7M martensite was observed to be the predominant structure (Figure IV.19), which is consistent with SAD patterns taken via TEM (figs. IV.9, IV.13 & IV.14).
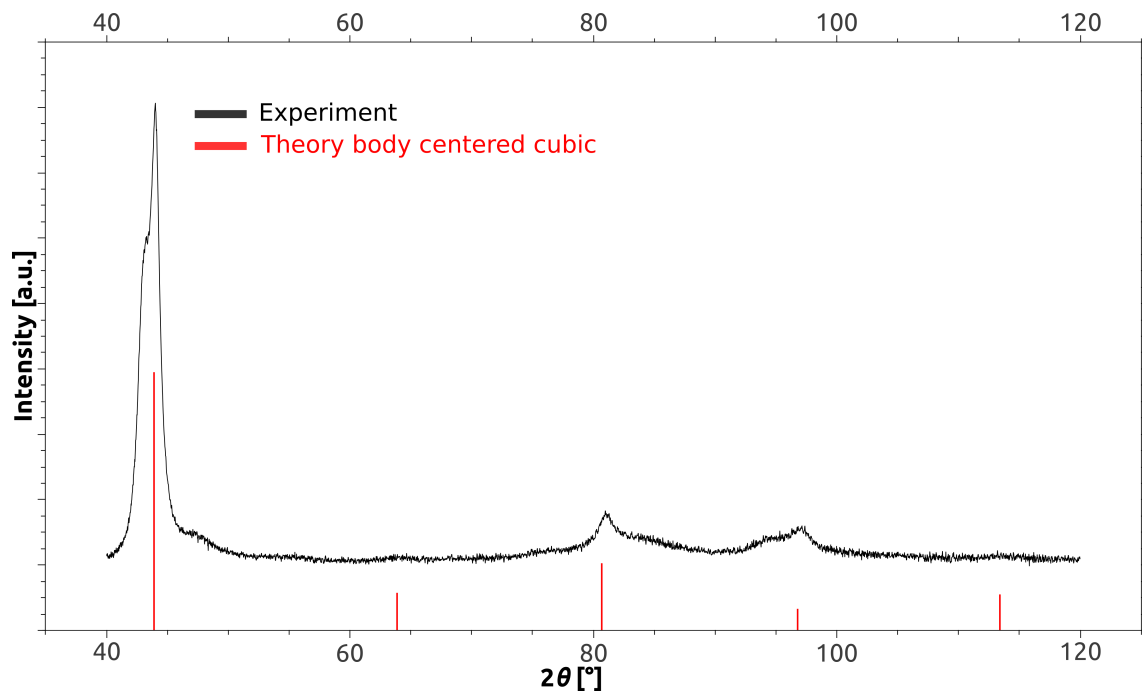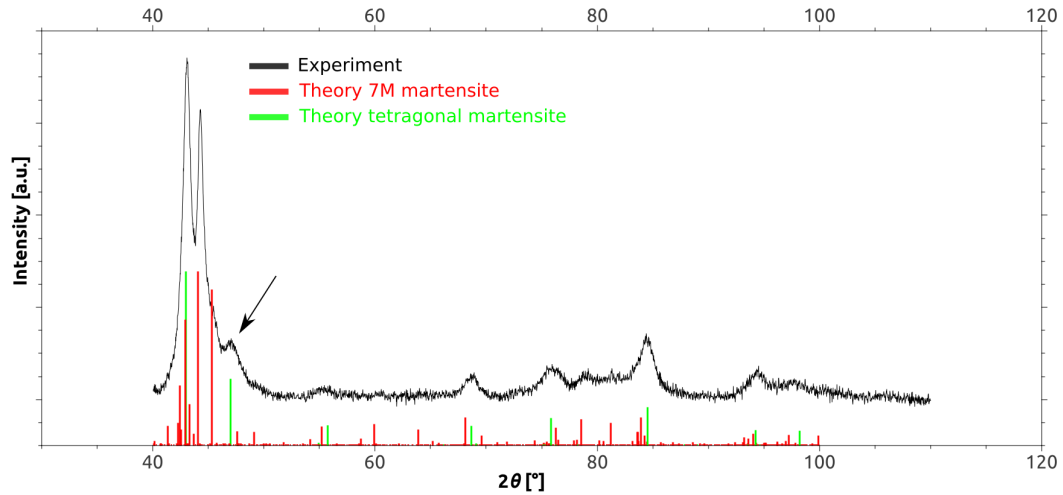
Figure IV.19: HPT deformed with heat treatment to a temperature of 500 °C (100 HTP-turns). Singular lines correspond to theoretical calculations. Metastable 7M martensite is observed (red), for purpose of camparison the theoretical reflexes of stable tetragonal martensite are shown additionally (green).

IV.3 DSC analysis

A 50 HPT-turns sample was chosen to conduct stepwise DSC analyses.

IV.3.1 Coarse grained

In Figure IV.20 the DSC analysis of the coarse grained material is shown. Due to the very clear peak it was easy to calculate the temperatures shown in IV.1. Still, the given numbers are rounded and only exact to about 1 °C due to the usage of the tangent method (unless indicated otherwise).
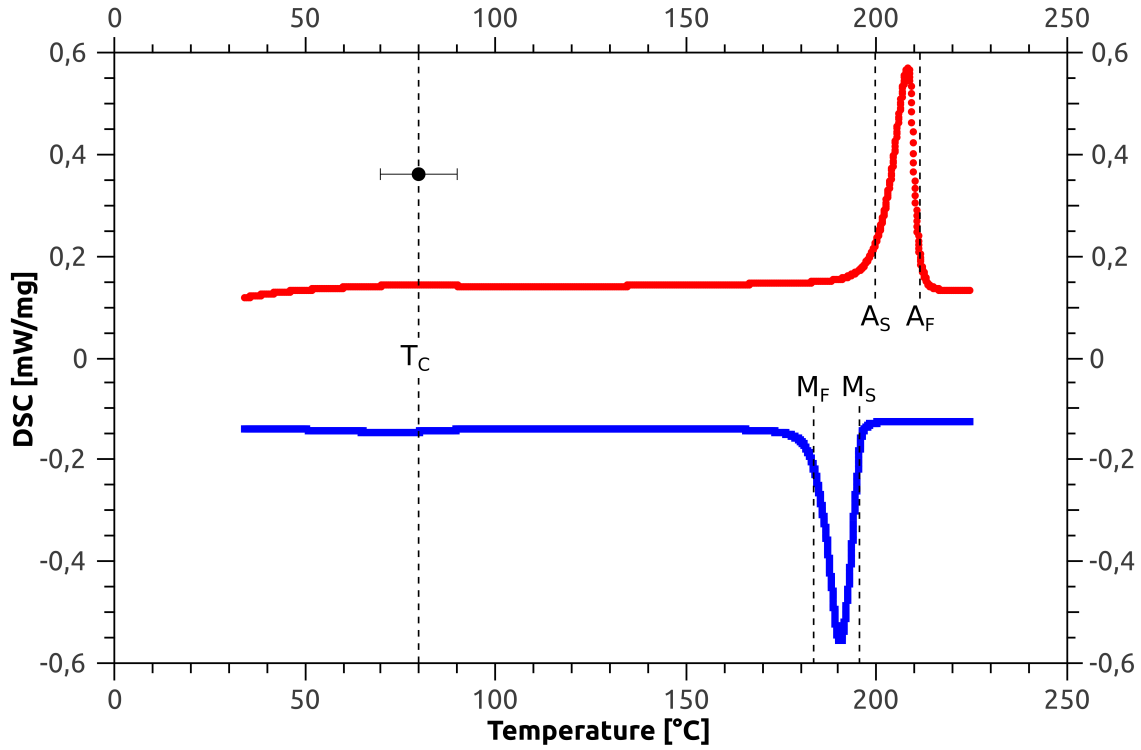
Figure IV.20: DSC analysis of coarse grained $Ni_{54}Mn_{25}Ga_{21}$. For the measured values refer to Table IV.1.

Austenite Start	$\mathbf{A_S}$	200 °C
Austenite Peak	$\mathbf{A_P}$	208 °C
Austenite Finish	$\mathbf{A_F}$	211 °C
Martensite Start	$\mathbf{M_S}$	196 °C
Martensite Peak	$\mathbf{M_P}$	190 °C
Martensite Finish	$\mathbf{M_F}$	184 °C
Curie Temp.	$\mathbf{T_C}$	80 ± 10 °C
Enthalpy (2M → L2$_1$)	$\mathbf{H_A}$	10 ± 0.5 J/g
Enthalpy (L2$_1$ → 2M)	$\mathbf{H_M}$	−10 ± 0.5 J/g

Table IV.1: Key values of the coarse grained material. The error is in the range of ± 1 °C (unless indicated otherwise).

IV.3.2   HPT deformation

At room temperature, the encountered fct and fcc phases are metastable. Upon isochronal heating to a temperature of 220 °C and subsequent cooling to room temperature no martensitic transformation takes place, i.e. neither an endothermic peak corresponding to the formation of austenite nor an exothermic peak corresponding to the formation of martensite was encountered in the DSC curves (Figure IV.21).

Additionally the transition from paramagnetic to ferromagnetic (heating) as well as that from ferromagnetic to paramagnetic (cooling) does not occur (no Curie temperature peak). This is due to the presence of the disordered fct and fcc structures.
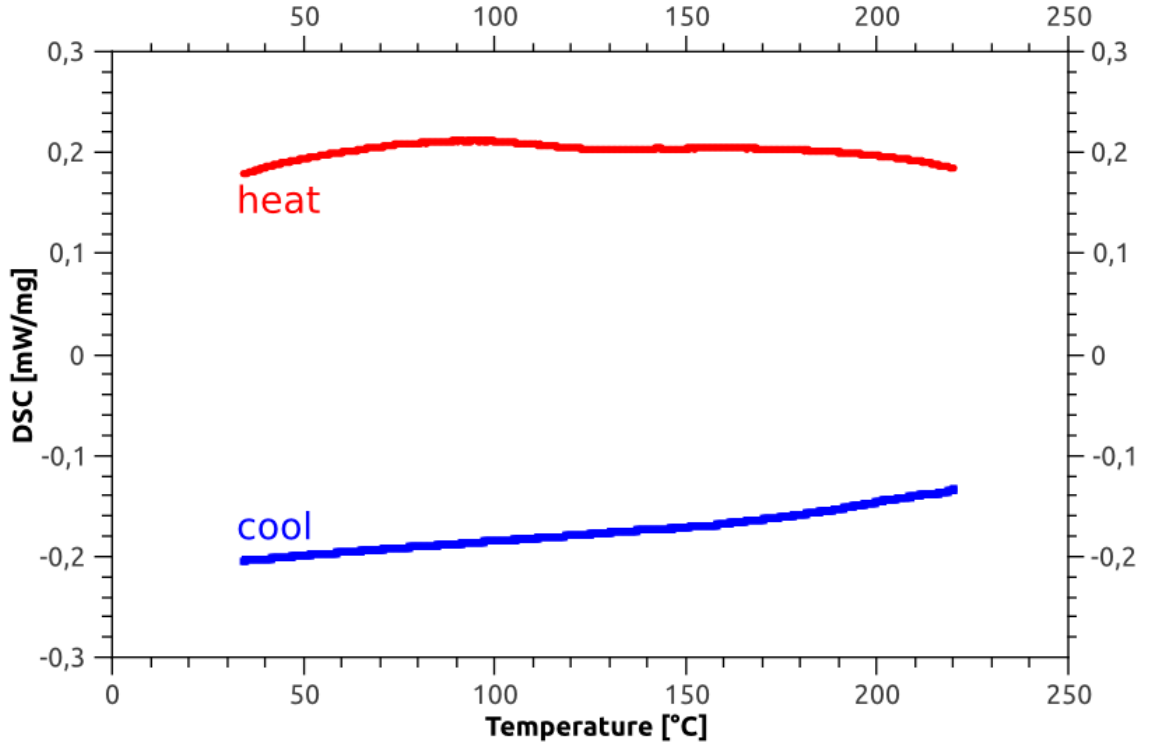
Figure IV.21: DSC analysis of HPT deformed $Ni_{54}Mn_{25}Ga_{21}$. No martensitic transformation takes place both upon heating and cooling.

IV.3.3   Isochronal heat treatments

Upon heating isochronally to a temperature of 420 °C a phase transformation with an exothermic peak at about 357 °C occurs (Figure IV.22). It was identified as disordered fcc/fct $\rightarrow$ disordered bcc. The disorder causes a supression of the martensitic transformation as well as the transition from paramagnetic to ferromagnetic upon cooling to room temperature (green curve, Figure IV.23).

After isochronal heating to 500 °C the martensitic transformation returns. The additional smaller peak corresponds to the Curie temperature (blue curve, Figure IV.23).
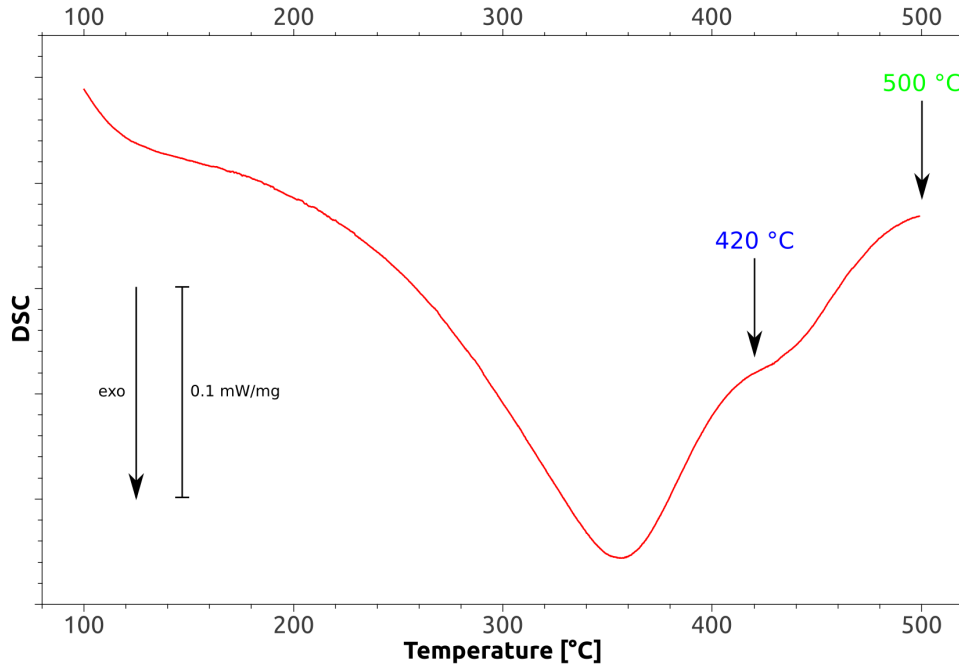
Figure IV.22: DSC heating curve. In different steps the HPT deformed sample was first heat treated to a temperature of 420 °C (the end of the first ordering peak) and cooled down. Afterwards heat treatment to a temperature of 500 °C and cooled down. For cooling curves see Figure IV.23.
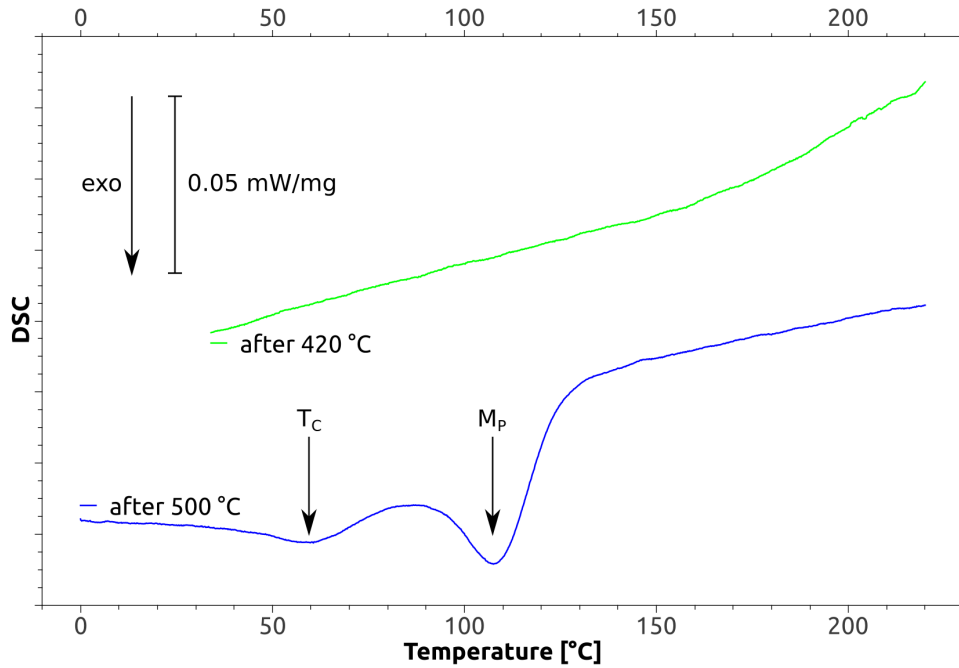
Figure IV.23: DSC cooling curves after isochronal heating to a temperature of 420 °C and 500 °C. After isochronal heat treatment to a temperature of 420 °C no martensitic transformation takes place (green). After isochronal heating to a temperature of 500 °C the martensitic transformation returns (blue). M_p: martensite start temperature. T_C: Curie temperature.

IV.3.4 Isothermal heat treatments

| #	500 °C	550 °C	590 °C	625 °C	650 °C	675 °C
1	10 Min	-	-	-	-	-
2	150 Min	-	-	-	-	-
3	150 Min	165 Min	-	-	-	-
4	150 Min	165 Min	40 Min	-	-	-
5	150 Min	165 Min	40 Min	30 Min	-	-
6	150 Min	165 Min	40 Min	30 Min	60 Min	-
7	150 Min	165 Min	40 Min	30 Min	60 Min	60 Min

Table IV.2: Key to steps of heat treatment.

Several isothermal treatments were conducted. In Table IV.2 the respective temperatures and times of the isothermals are listed together with the sample numbers (#1, #2, ...) which are used in the following graphs and tables. The given numbers are *only* the accumulated isothermals neglecting the isochronal heating and cooling (20 K/minute) in between.

In Table IV.3 and Table IV.4 the different measured temperature and enthaply values are listed. Ther error of the temperature values constitutes to about ± 3 °C due to the smearead peaks and the use of the tangent method. The error of the enthalpy values is in the range of up to 20% (about ± 0.5 J/g). Certain values of the Curie temperature T_C are given as not available (n.a.) because the respective DSC curves did not show a significant peak from which it could have been inferred.

The "small cycle" shown in the DSC curves in Figure IV.24 were done after the respective accumulated isothermals. The range of this "small cycle" was from a temperature of -50 °C to a temperature of 200 to 240 °C (and back), depending on the previous heat treatment and thus the temperature where the austenitic transition was expected to be complete. An increase of the transformation temperatures and enthalpies can be observed due to heat treatment, which - for the transformation temperatures - is even more clearly observable in Figure IV.25.

#	A_s	A_p	A_f	M_s	M_p	M_f	T_C heat	T_C cool
1	106	132	151	130	120	102	66	n.a.
2	120	154	170	148	137	109	71	51
3	141	170	181	162	152	128	71	61
4	150	174	184	166	157	135	73	58
5	157	180	188	170	162	142	69	61
6	160	187	195	175	169	145	n.a.	n.a.
7	173	192	199	181	175	161	n.a.	n.a.

Table IV.3: Temperature values in [°C], error ±1 °C. For sample key (#1, #2, etc.) refer to Table IV.2.

#	H_A	H_M	$|\overline{H}|$
1	2.4	-2.4	2.4
2	3.0	-3.0	3.0
3	3.0	-3.3	3.2
4	3.3	-3.5	3.4
5	3.9	-4.0	4.0
6	6.4	-6.4	6.4
7	5.6	-5.8	5.7

Table IV.4: Enthalpy values in [J/g], error ±0.5 J/g. For sample key (#1, #2, etc.) refer to Table IV.2.
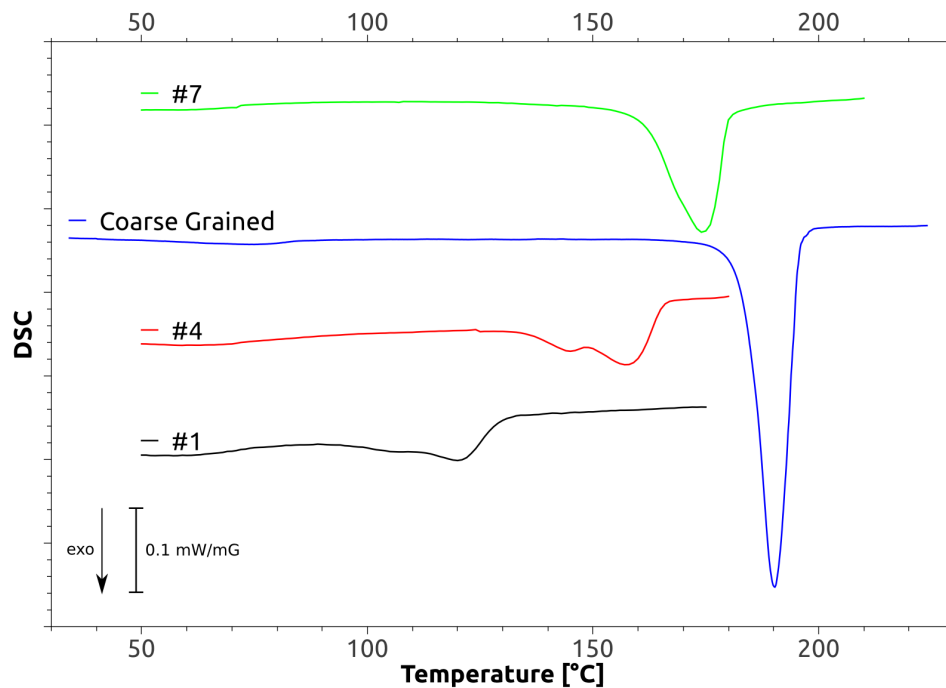

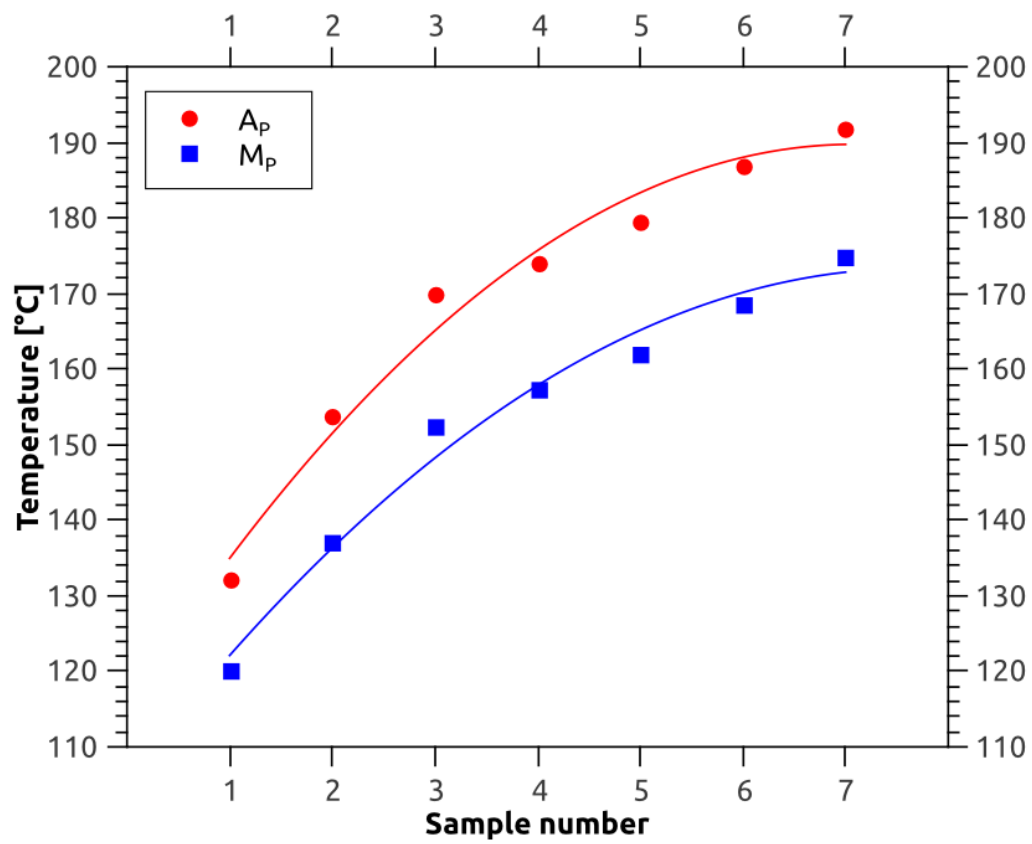**Figure IV.24:** Comparison of DSC analyses. For sample key (#1, #4, etc.) refer to Table IV.2.

Figure IV.25: Shift of austenite and martensite peak temperatures (A_P, M_P) due to heat treatment. For the key to the sample number refer to Table IV.2.

Chapter V

Discussion

V.1 General remarks

The different lattice structures 2M, fct, fcc, bcc and 7M were clearly identified via TEM and XRD. However lattice parameters calculated from TEM SAD images are only accurate within a deviation of about 10%. This is due to a systematical error of about 5%, e.g. arising by the lack of accurate reproducibility of calibration caused by the remanescence of magnetic lenses. Another 5% are from the stochastic error, e.g. the accuracy of identifying the exact positions of the Bragg reflection peaks in TEM SAD images. Also, the degree of order was not observed directly, since intensity of superstructure reflections in TEM SAD and XRD is very low. This is due to Ni, Mn and Ga being very close in the Periodic Table of Elements and thus possessing nearly identical atomic form factors. A very reliable method to ascertain the degree of order is neutron scattering (see Brown et al.[30]) which wasn't conducted in the course of this work.

V.2 Initial State and HPT deformation

The coarse grained $Ni_{54}Mn_{25}Ga_{21}$ alloy in its initial state analyzed by TEM and XRD showed an ordered 2M unmodulated tetragonal martensite (Figures IV.2 & IV.16). This agrees with literature[31]. The lattice parameters are listed in Table V.1.

(i)	a	c	c/a
Experiment	0.82	0.69	0.84
Ref. [14]	0.77	0.67	0.87

(ii)	a	c	c/a
Experiment	0.73	0.63	0.86
Ref. [29]	0.78	0.65	0.83

(iii)	a
Experiment	0.35
Ref. [29]	0.37

Table V.1: Lattice parameters in [nm] of:
(i) tetragonal martensite, (ii) disordered fct and (iii) γ-phase.

Considering the sources of error the variations are well within within a reasonable deviation. The difference of c/a-ratio of the tetragonal phases where only the stochastic error constitutes is only at about 2.3%, which suggests no significant decrease in lattice parameters after HPT deformation.

The phase transformation temperatures of the coarse grained material $A_f = 200°C$ and $M_s = 196°C$ were lower than those presented by Ma et al. with $A_f = 288.1°C$ and $M_s = 260.2°C$[31] (see also Table IV.1), but these temperatures are extremely sensitive to even slight changes in stoichiometric composition (a change of 1%-at. results in up to ±100 °C), which puts this variation well within a reasonable deviation caused by imprecision in composition (see Section III.1). The forward martensitic phase transition of the undeformed material can thus be described as $L2_1 \rightarrow 2M$.

After HPT two phases were detected: disordered fct (disordered 2M martensite) and γ-phase (disordered fcc) (Figures IV.5 & IV.17). The respective lattice parameters calculated via TEM SAD (combined with literature values for comparison) can be seen in Table V.1. Therefore it is concluded that HPT destroys the order of the martensite. Destruction of the long range chemical order by methods of severe plastic deformation (SPD) is frequently observed in intermetallic alloys; the decrease of the chemical order is proposed to be caused by a high density of dislocations that

are induced by the SPD and show a specific dissociation scheme[32, 33, 34]. While in the present work the degree of chemical order was not measured by means of electron diffraction and XRD (see Section V.1), the conlusion of chemical disordering is based on the following experimental observations: firstly due to the lack of a martensitic reverse transformation, that is: martensite to austenite (Figure IV.21). Secondly because the competing γ-phase is stabilized at the account of the tetragonal phase (Figure IV.5). Occurence of the γ-phase is not unusual in Ni-Mn-Ga alloys, especially in those with higher Ni concentrations[31]. Since off stoichiometric compositions must have anti sites or vacancies to compensate for higher or lower numbers of atoms of a respective element, the degree of order is lower than that in the stoichiometric composition. It can thus be concluded that the stabilization of the γ-phase is a reliable indication for a decrease in the degree of order induced by HPT. Both phases - disordered fct as well as γ phase - were reported to occur in ball milled $Ni_{49.8}Mn_{28.5}Ga_{21.7}$, but not coexistent: planetary ball milling *only* showed disordered fct whereas vibrational ball milling *only* showed disordered fcc[29, 35]. Wang et al. also reported the occurrence of disordered fcc, but together with an amorphous phase[36] which was not reproduced within the presented work.

While the initial material showed coarse grains, HPT of Ni-Mn-Ga alloys can induce significant grain refinement (Figure IV.3). A nanocrystalline structure is typically obtained when all the grains have a size of 100 nm or less[37]. Using HPT, various intermetallic alloys can be rendered nanocrystalline[32]. Whereas in the present case even after the application of an excessive plastic strain most of the grain fragments have a size which is still slightly larger than 100 nm, and some larger fragments were encountered as well. In addition to the formation of a submicrocrystalline structure, grain refinement seems to occur mainly by the formation of low angle subgrain boundaries. Within the framework of the present thesis, the physical reasons for the limited grain refinement were not elucidated. There might be some processes of dynamical recovery that limit the final grain size and hinder the formation of large angle grain boundaries. It should be noted that in the case of SPD by HPT and ball milling lower grain sizes (e.g. 10 to 20 nm) and even amor-

phization were claimed to occur in NiMnGa based alloys of a composition similar to that used in the present thesis[36, 38]. The reason for this discrepancy might be based on the different values of the hydrostatic pressure applied during HPT. While in the present thesis a pressure of 8 GPa was used, the hydrostatic pressure used by Kourov et al. is in the range of 3 to 5 GPa[39]. However, attempts to apply a rather low value of the hydrostatic pressure (4 GPa) during the course of the present work failed since the material showed fracture a rather low degree of plastic deformation.

V.3   Structural transitions during annealing

During the isochronal heat treatment the heavily deformed ultrafine grained structure of the HPT samples transforms into a microstructure containing well defined polygonal grains that show little lattice strains (Figure IV.10). Based on the experimental results it is concluded that the heat treatment causes recrystallization that occurs by the nucleation of small grains (see Figure IV.6 where at an intermediate temperature already new grains have nucleated and grown on the expense of the highly deformed matrix). In addition, lattice strains are substantially reduced by mechanisms of recovery including the recombination of dislocations induced by the HPT. Similar mechanisms of recrystallization and recovery were observed in the case of deformed NiTi shape memory alloys[40]. It is important to note that the isochronal heat treatment up to a temperature of 500°C does not yield significant grain growth.

Since the disordered fct/fcc phases of the HPT deformed material are metastable, it can be expected that heat treatment causes (re)ordering to thermodynamically more stable structures. Additionally it will lead to the recombination of dislocations and the reduction of lattice strains. This process was observed by DSC and is interpreted as follows. Upon heating two distinct irreversible processes were observed: the DSC signal showed two overlapping exothermal peaks, one at about 357 °C and one at about 420 °C (see Figure IV.22). The 357 °C-peak seems to be a structural transition from γ-phase and disordered fct to disordered bcc. This is further confirmed by the microstructural analyses via TEM SAD (whereof the bcc

lattice parameter was calculated as $a = 0.28$ nm) and as X-ray (see Figures IV.8 & IV.18). Additionally there is a lack of an exothermic peak in the DSC cooling curve after isochronal heating to a temperature of 420 °C (Figure IV.23), thus no martensitic transformation takes place. Using planetary ball milling as technique to obtain SPD, Tian et al. reached similar results with $Ni_{49.8}Mn_{28.5}Ga_{21.7}$[41].

The second DSC peak at 420 °C was identified as the transformation from disordered bcc to the highly ordered $L2_1$ Heusler austenite. This is confirmed by the reapperance of a forward martensitic transformation peak (austenite → martensite) upon cooling to room temperature.

Concerning the martensitic transformation, significant changes are observed compared to the coarse grained and the HPT deformed material. Firstly the DSC signal shows that the transformation is still supressed to an amount, resulting in the drop of the martensitic transformation temperatures (see Figure IV.25 & Tables IV.1, IV.3) and transformation enthalpies (see Tables IV.1, IV.4). Secondly the lattice structure changes in the way that a different type of martensite is stabilized: contrary to the 2M martensite found in the coarse grained material, the metastable modulated 7M variant is now observed to be predominant (see Figures IV.9 & IV.19). This is believed to be caused by the decrease of grain size (see Waitz et al.[4]). The martensite is confined by the grain boundaries, thus making them phase boundaries ("martensitic inclusions"). When grains become smaller their surface-to-volume ratio increases thus making the terms of the martensite's strain energy scaling with surface non-negligible. For a given martensitic structure strains can be accomodated by twinning. Part of the transformation strains are located at the surface of the martensitic inclusion and thus are scaling with the surface area. The fraction of the transformation strains scaling with the surface area can be minimized by a decrease in twin width (minimizing the range of those strains located at the surface). However, a decrease of the twin width yields an increase of the total twin boundary area per unit of transformed volume. This can only be counterbalanced by a low *specific* twin boundary energy, which is fulfilled by an adaptive martensite[17, 42]. In

the case of Ni-Mn-Ga such an adaptive martensitic structure was recently proposed to occur. This adaptive martensitic structure is the 7M modulated martensite that is experimentally observed in the present case of the nanograins.

With respect to their free enthalpy in the coarse grains, both the free enthalpy of the 2M and 7M martensitic structures will increase with decreasing grain size at a submicron scale. In the small grains, the additional enthalpy that arises by strain and interface energy is denoted by ΔH_{2M} and ΔH_{7M} for the 2M and 7M martensite, respectively (see Figure V.1). While both ΔH_{2M} and ΔH_{7M} will increase with decreasing grain size, it is expected that $\Delta H_{7M} < \Delta H_{2M}$, since in small grains the adaptive 7M martensite shows an optimized configuration minimizing the transformation strain and interface energy. Also, as compared to ΔH_{2M}, it is expected that ΔH_{7M} will increase less with grain size. Therefore, upon cooling of grains smaller than a critical size, the austenite will transform to the 7M martensite first (at a temperature T_3); upon further cooling the 7M martensite might transform into the 2M martensite (it should be noted that the corresponding temperature T_5 might be well below room temperature; corresponding low temperature DSC experiments were not carried out in the framework of the present thesis).

An experimental indication for a low specific twin boundary energy is found in the nanostructure of the 7M martensite. From a perfect $(5\bar{2})$ stacking sequence a sinusoidal variation of contrast would be expected in lattice fringe imaging (see Section III.3.3). Deviation from a perfect sinusoidal pattern arises from a deviaion in stacking sequence which is experimentally observed (see Figures IV.12, IV.15). This causes stacking faults at the same crystallographic planes that act as twinning planes of the 2M martensite. Since the number density of these stacking faults is quite high, it is concluded that the specific stacking fault energy (and thus the specific twin boundary energy) is rather low. It can be said that the free enthalpy of the respective martensites is increased by ΔH due to a decrease in grain size, resulting - in this work - in the stabilization of 7M martensite in the ultra fine grained material at the account of 2M martensite (see Figure V.1).
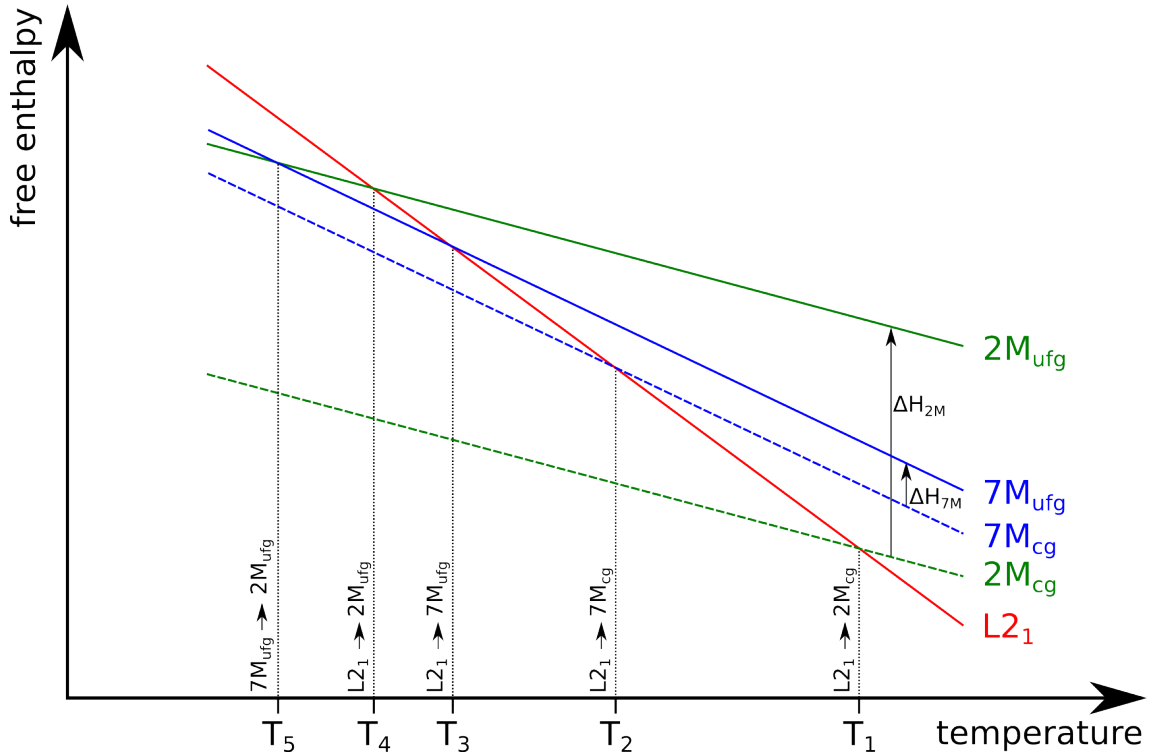
Figure V.1: Favoured phase transformations, comparing coarsed grains ($2M_{cg}$, $7M_{cg}$) and ultra fine grains ($2M_{ufg}$, $7M_{ufg}$). With decreasing grain size transformation free enthalpies are hightened by an increase of enthalpy (ΔH_{2M} & ΔH_{7M}) mainly caused by strain energy. 7M martensite is stabilized at certain temperatures (between T_3 and T_5) at the account of 2M martensite. The transformations at T_2 and T_4 are hypothetical and do not occur.

	heating	cooling
as received	$2M \rightarrow L2_1$	$L2_1 \rightarrow 2M$
HPT	diso. fct/fcc $\nrightarrow$	diso. fct/fcc $\nrightarrow$
HPT + HT 420 °C	diso. fct/fcc $\rightarrow$ diso. bcc	diso. bcc $\nrightarrow$
HPT + HT 500 °C	diso. fct/fcc $\rightarrow$ diso. bcc $\rightarrow L2_1$	$L2_1 \rightarrow 7M$

Table V.2: Structural evolution due to HPT and heat treatment (HT).
$\rightarrow \ldots$ phase transformation to / $\nrightarrow \ldots$ no phase transformation

HPT and and subsequent heat treatment to a temperature of 500 °C (Sample #1, see Table IV.2) rendered a significant drop of A_f and M_s to before HPT treatment. The longer the time of annealing combined with an increase of temperature, A_p and M_p increased again but even after an extended period of time and high temperatures (Sample #7, see Table IV.2) the values did not return to those of the starting material before HPT (see Figure IV.25 & Table IV.3).

Analyzing the DSC curves, two small but still clearly identifyable peaks were

observed besides those arising from the martensitic phase transformations: an endothermic peak in the heating curve and an exothermic one in the cooling curve. These peaks were observed in both the coarse grained as well as the utra fine grained material (see Figures IV.20, IV.23 & IV.24). Their characteristics were consistent with those of the transition from paramagnetic to ferromagnetic (heating) and vice versa (cooling)[43]. They were therefore identified as the peaks corresponding to the Curie temperature T_C. Since the peak temperatures occur between 59 and 72 °C it can be concluded that the martensitic phase (be it 2M or 7M) is ferromagnetic, while the austenite is paramagnetic. The peak enthalpies were in the range of 0.6±0.2 J/g and thus - if small - clearly observable in the DSC signal. This is very uncommon for ferromagnetic solids, where the enthalpies are usually considerably lower[44].

An effect of the decrease of grain size on the Curie temperature was not observed in the present work, but taken into account the weakness of the peak and the resulting inaccuracy of the determination (±10 °C), see Table IV.3) no definitive statement about an increase or decrease can be made.

Chapter VI

Summary and Conclusions

In the presented work the ferromagnetic shape memory alloy $Ni_{54}Mn_{25}Ga_{21}$ was subjected to HPT to obtain strong grain refinement. The structural evolution induced by HPT and after HPT followed by heat treatment was studied. The main emphasis of the present work was to elucidate the effect of the grain size on the martensitic phase transformations.

Different complementary experimental methods including TEM, DSC and XRD were used and described in Chapter III. Disc shaped specimen (diameter of 8 mm and thickness in the range of 0.7 ± 0.1 mm) for HPT were obtained from the initial alloy using spark erosion. The HPT was carried out at a pressure of 8 GPa. Samples were subjected to 50 or 100 turns of HPT resulting in degrees of deformation of $2.2 \cdot 10^5$ % and $5.8 \cdot 10^5$ % respectively. After that specimens with a diameter of 2.3 mm were punched form the HPT discs and used to prepare TEM samples. Samples were also subjected to different heat treatments in the DSC. Isochronal heating was carried out to a maximum temperature of 420 °C and 500 °C. Specimens isochonically heated to a temperature of 500 °C were also subjected to isothermal treatments at temperatures ranging from 500 to 675 °C for a time between 5 and 165 minutes. To obtain the thin samples suitable for TEM, specimens were dimpled until they reached a thickness of about 20 to 30 μm and finally subjected to ion thinning.

In Chapter IV the experimental results are shown. The initial material shows grain sizes of several hundreds of micrometers. After HPT deformation the struc-

ture was strongly fragmented mainly due to the formation of subgrain boundaries. These subgrain boundaries were hard to locate in the TEM bright and dark field images. Most of the observed fragments were spreading over several hundreds of nanometres and had largely uniform contrast. In addition however, some fragments were observed where the contrast varied on a smaller scale (120 ± 6 nm). After isochronal heat treatment to a temperature of 420 °C, signs of recrystallization by grain nucleation can be seen in the TEM bright field images. After heating to a temperature of 500 °C the process of recrystallization is almost complete and the TEM analysis shows well defined polygonal grains. The average diameter of those grains were assesed to be 140 ± 6 nm. It is therefore concluded that, although Ni-Mn-Ga alloys are rather brittle, HPT can be applied successfully to yield strong grain refinement in the bulk material.

At room temperature the unmodulated tetragonal 2M martensite was observed in the coarse grained material . HPT induced strong chemical disorder yielding an fct structure. In addtion, a deformation induced phase transformation occurs since the disordered fcc γ-phase was encountered after HPT. Caused by the strong disordering of the martensitic phase and by the formation of the fcc structure, upon heating a reverse martensitic transformation yielding the formation of austenite was not observed. However, upon isochronal heating to a temperature of 420 °C a strong peak occured in the DSC signal at a temperature of ca. 357 °C. This peak corresponds to a structural transition from fct/fcc to a disordered bcc lattice structure. Upon cooling to room temperature, the bcc structure was stable. This is due to the chemical disorder that completely impedes the forward martensitic transformation.

HPT specimens heated isochronically to a temperature of 500 °C showed a martensitic phase transformation both upon cooling and heating. Therefore, it is concluded that by this heat treatment the bcc to austenite transformation has occurred by ordering. Since by heating the $L2_1$ Heusler austenitic structure is obtained prior to the onset of significant grain growth the impact of the submicrocrystalline structure on the martensitic phase transformation can be studied. As a result,

upon cooling from the austenite the modulated adaptive 7M martensite is formed in the small grains. Therefore, the 7M martensite occurs at the account of the unmodulated 2M martensite observed in the coarsed grains. Moreover, the phase transformation temperatures observed in the ultrafine grained structure are significantly lower (about 100 °C) than those observed in the coarse grained structure. Interestingly the transformation temperatures are not fully recovered even after annealing for 165 minutes at a temperature of 675 °C although by this heat treatment coarsed grains are expected to occur.

A single variant of the 7M martensite frequently containing stacking faults is observed in most of the grains. However, in some grains a twinned morphology of the 7M martensite occurs. The suppression of the 2M martensite and the occurrence of the modulated 7M structure is caused by the influence of the grain size on the free enthalpy. In addition to the phase stability, the morphology of the martensite can be explained in terms of the impact of grain size on its free enthalpy. The most important conclusion to be taken from this thesis is that in the ultrafine grains the metastable, modulated, adaptive 7M martensite to show an optimized accommodation of the transformation strains.

Acknowledgement

Bibliography

[1] J Enkovaara, A Ayuela, AT Zayak, P Ente, L Nordstrom, M Dube, J Jalkanen, J Impola, and RM Nieminen. Magnetically driven shape memory alloys. *Materials Science and Engineering A - Structural Materials Properties Microstructure and Processing*, 378(1-2, Sp. Iss. SI):52–60, Jul 25 2004. European Symposium on Martensitic Transformation and Shape-Memory, Cirencester, England, 2003.

[2] A Sozinov, AA Likhachev, N Lanska, and K Ullakko. Giant magnetic-field-induced strain in NiMnGa seven-layered martensitic phase. *Applied Physics Letters*, 80(10):1746–1748, 2002.

[3] K. Otsuka and C.M. Wayman, editors. *Shape Memory Materials*. Cambridge University Press, 1998.

[4] T. Waitz, T. Antretter, F.D. Fischer, N.K. Simha, and H.P. Karnthaler. Size effects on the martensitic phase transformation of NiTi nanograins. *Journal of the Mechanics and Physics of Solids*, 55(2):419 – 444, 2007.

[5] G. B. Olson and W. S. Owen, editors. *Martensite*. AMS International, 1992.

[6] RD James and M Wuttig. Magnetostriction of martensite. *Philosophical Magazine A*, 77(5):1273–1299, 1998.

[7] AN Lavrov, S Komiya, and Y Ando. Magnetic shape-memory effects in a crystal. *Nature*, 418(6896):385–386, 2002.

[8] Manfred Wuttig, Jian Li, and Corneliu Craciunescu. A new ferromagnetic shape memory alloy system. *Scripta Materialia*, 44(10):2393 – 2397, 2001.

[9] K Ullakko, JK Huang, C Kantner, RC O'Handley, and VV Kokorin. Large magnetic-field-induced strains in Ni_2MnGa single crystals. *Applied Physics Letters*, 69(13):1966–1968, 1996.

[10] Charles Kittel. *Introduction to Solid State Physics*. John Wiley & Sons, 8th edition, 2004.

[11] D.B. Williams and C.B. Carter. *Transmission Electron Microscopy*. Springer, 1996.

[12] L Righi, F Albertini, A Paoluzi, S Fabbrici, E Villa, G Calestani, and S Besseghini. Incommensurate and commensurate structural modulation in martensitic phases of FSMA. *Materials Science Forum*, 635:33–41, 2010.

[13] Tanja Graf, Claudia Felser, and Stuart S.P. Parkin. Simple rules for the understanding of Heusler compounds. *Progress in Solid State Chemistry*, 39(1):1 – 50, 2011.

[14] C Jiang, G Feng, S Gong, and H Xu. Effect of Ni excess on phase transformation temperatures of NiMnGa alloys. *Materials Science and Engineering A*, 342(1-2):231–235, 2003.

[15] Seda Aksoy. *Magnetic interactions in martensitic Ni-Mn based Heusler systems*. PhD thesis, Universität Duisburg-Essen, 2010.

[16] J. Pons, V.A. Chernenko, R. Santamarta, and E. Cesari. Crystal structure of martensitic phases in Ni-Mn-Ga shape memory alloys. *Acta Materialia*, 48(12):3027–3038, 2000. cited By (since 1996) 340.

[17] S. Kaufmann, U. K. Roessler, O. Heczko, M. Wuttig, J. Buschbeck, L. Schultz, and S. Faehler. Adaptive Modulations of Martensites. *Physical Review Letters*, 104(14), 2010.

[18] R.C. Pond, B. Muntifering, and P. Müllner. Deformation twinning in Ni_2MnGa. *Acta Materialia*, 60(9):3976 – 3984, 2012.

[19] L Righi, F Albertini, E Villa, A Paoluzi, G Calestani, V Chernenko, S Besseghini, C Ritter, and F Passaretti. Crystal structure of 7M modulated Ni-Mn-Ga martensitic phase. *Acta Materialia*, 56(16):4529–4535, 2008.

[20] L Righi, F Albertini, L Paret, A Paoluzi, and G Calestani. Commensurate and incommensurate "5M" modulated crystal structures in Ni-Mn-Ga martensitic phases. *Acta Materialia*, 55(15):5237–5245, 2007.

[21] C. Mangler, T. Waitz, and P. Müllner. Severe plastic deformation of high temperature Ni-Mn-Ga shape memory alloys studied by TEM and DSC. In *3rd International Conference on Ferromagnetic Shape Memory Alloys, Dresden*, 2011.

[22] J. Enkovaara, A. Ayuela, L. Nordström, and R. M. Nieminen. Magnetic anisotropy in Ni_2MnGa. *Phys. Rev. B*, 65:134422, Mar 2002.

[23] J. Enkovaara, A. Ayuela, L. Nordstrom, and R. M. Nieminen. Structural, thermal, and magnetic properties of Ni_2MnGa. *Journal of Applied Physics*, 91(10):7798–7800, 2002.

[24] V. G. Pushin, A. V. Korolev, N. I. Kourov, D. V. Gunderov, R. Z. Valiev, V. V. Koledov, and V. G. Shavrov. *SPD-induced nanocrystallization of shape memory Ni_2MnGa-based and NiTi-based alloys quenched from liquid state*, volume 503-504 of *Materials Science Forum*. 2006.

[25] P. Schindler. Quantum Confined Structures for High Efficiency Solar Cells Studied by Transmission Electron Microscopy. Master's thesis, University of Vienna, 2011.

[26] Patrick Echlin. *Handbook of Sample Preparation for Scanning Electron Microscopy*. Springer, 1st edition, 2009.

[27] G. Höhne, W. Hemminger, and H.-J. Flammersheim. *Differential Scanning Calorimetry An Introduction for Practitioners*. Springer-Verlag Berlin Heidelberg, 1996.

[28] T Waitz and C Mangler. Private communication.

[29] B. Tian, F. Chen, Y. X. Tong, L. Li, Y. F. Zheng, Y. Liu, and Q. Z. Li. Phase transition of Ni-Mn-Ga alloy powders prepared by vibration ball milling. *Journal of Alloys and Compounds*, 509(13):4563–4568, 2011.

[30] PJ Brown, J Crangle, T Kanomata, M Matsmuoto, KU Neumann, B Ouladdiaf, and KRA Ziebeck. The crystal structure and phase transitions of the magnetic shape memory compound Ni_2MnGa. *Journal of Physics - Condensed Matter*, 14(43):10159–10171, 2002.

[31] Yunqing Ma, Chengbao Jiang, Yan Li, Huibin Xu, Cuiping Wang, and Xingjun Liu. Study of $Ni_{50+x}Mn_{25}Ga_{25-x}$ ($x = 2$-11) as high-temperature shape-memory alloys. *Acta Materialia*, 55(5):1533–1541, 2007.

[32] A.P. Zhilyaev and T.G. Langdon. Using high-pressure torsion for metal processing: Fundamentals and applications. *Progress in Materials Science*, 53(6):893 – 979, 2008.

[33] C. Gammer, C. Mangler, H.P. Karnthaler, and C. Rentenberger. Growth of nanosized chemically ordered domains in intermetallic FeAl made nanocrystalline by severe plastic deformation. *Scripta Materialia*, 65(1):57 – 60, 2011.

[34] D. Geist, C. Gammer, C. Mangler, C. Rentenberger, and H. P. Karnthaler. Electron microscopy of severely deformed $L1_2$ intermetallics. *Philosophical Magazine*, 90(35-36):4635–4645, 2010.

[35] F Chen, B Tian, L Li, and Y-F Zheng. Structural transition of Ni-Mn-Ga ferromagnetic shape memory alloy particles prepared by ball milling. *Transactions of Nonferrous Metals Society of China*, 17(Part b, 1):S614–S617, Nov 2007. International Conference of Nonferrous Materials (ICNFM), Changsha, Peoples Rep. of China, Nov 25-30, 2007.

[36] Y. D. Wang, Y. Ren, Z. H. Nie, D. M. Liu, L. Zuo, H. Choo, H. Li, P. K. Liaw, J. Q. Yan, R. J. McQueeney, J. W. Richardson, and A. Huq. Structural

transition of ferromagnetic Ni_2MnGa nanoparticles. *Journal of Applied Physics*, 101(6), 2007.

[37] H.-J. Fecht. *Nanomaterials by Severe Plastic Deformation.* WILEY-VCH, 2004.

[38] N. I. Kourov, V. G. Pushin, A. V. Korolev, V. V. Marchenkov, E. B. Marchenkova, V. A. Kazantsev, and H. W. Weber. Effect of severe plastic deformation by torsion on the properties and structure of the $Ni_{54}Mn_{21}Ga_{25}$ and $Ni_{54}Mn_{20}Fe_1Ga_{25}$ alloys. *Physics of the Solid State*, 53(1):91–99, 2011.

[39] N. Kourov, V. Pushin, A. Korolev, V. Kazantsev, E. Marchenkova, and A. Uksusnikov. Effect of severe plastic deformation on the structure and properties of the $Ni_{2.16}Mn_{0.84}Ga$ alloy. *The Physics of Metals and Metallography*, 103:270–277, 2007.

[40] B. Malard, J. Pilch, P. Sittner, R. Delville, and C. Curfs. In situ investigation of the fast microstructure evolution during electropulse treatment of cold drawn NiTi wires. *Acta Materialia*, 59(4):1542 – 1556, 2011.

[41] B. Tian, F. Chen, Y. Liu, and Y. F. Zheng. Structural transition and atomic ordering of $Ni_{49.8}Mn_{28.5}Ga_{21.7}$ ferromagnetic shape memory alloy powders prepared by ball milling. *Materials Letters*, 62(17-18):2851–2854, 2008.

[42] A. G. Khachaturyan, S. M. Shapiro, and S. Semenovskaya. Adaptive phase formation in martensitic transformation. *Phys. Rev. B*, 43(13):10832–10843, May 1991.

[43] Hongxing Zheng, Dianzhen Wu, Sichuang Xue, Jan Frenzel, Gunther Eggeler, and Qijie Zhai. Martensitic transformation in rapidly solidified Heusler $Ni_{49}Mn_{39}Sn_{12}$ ribbons. *Acta Materialia*, 59(14):5692 – 5699, 2011.

[44] Ingale Babita, M. Manivel Raja, R. Gopalan, V. Chandrasekaran, and S. Ram. Phase transformation and magnetic properties in Ni-Mn-Ga Heusler alloys. *Journal of Alloys and Compounds*, 432(1-2):23–29, 2007.

Curriculum Vitae

Personal Information

Full name:	Arno Emanuel Kompatscher
Place of birth:	Hall in Tirol, Austria
Date of birth:	June 4th, 1984
Nationality:	Austria
E-mail:	arno@kompatscher.at
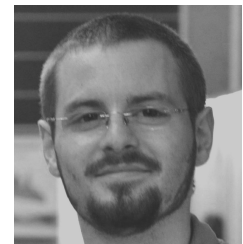
Education & Practical Experience

since 05.2011	Diploma student in Transmission Electron Microscopy Research group "Physics of Nanostructured Materials" University of Vienna, Austria
07.2010	Contractor Experimental Basic Training University of Vienna, Austria
07.2007 - 06.2011	Representative Austrian Student Union (ÖH) Vienna, Austria
07. - 09.2008	Internship R&D Diamond Consumables, Hilti Corporation Schaan, Liechtenstein
02. - 06.2007	Technical assistant in quantum optics research Institute for Quantum Optics & Quantum Information (IQOQI) Austrian Academy of Sciences (ÖAW) Vienna, Austria
08.2004 - 01.2007	Technical assistant in quantum optics research Institute of Experimental Physics University of Vienna, Austria
since 10.2003	Undergraduate studies in physics (equivalent to M.Sc.) University of Vienna, Austria
06.2003	High school graduation with merit Privatgymnasium Mehrerau Bregenz, Austria

Conference Proceedings

MC 2011, Kiel, GER:	*"TEM investigation of ferromagnetic shape memory alloys subjected to severe plastic deformation"* C. Mangler, <u>A.E. Kompatscher</u>, P. Müllner, T. Waitz

Scientific Conferences & Talks

Poster Presentation:	MC 2011, Kiel, GER: *"TEM investigation of ferromagnetic shape memory alloys subjected to severe plastic deformation"* C. Mangler, <u>A.E. Kompatscher</u>, P. Müllner, T. Waitz
Oral Presentation:	Seminar Micro- & Nanomaterials (2011), Vienna, AUT: *"Ni$_{54}$Mn$_{25}$Ga$_{21}$ ferromagnetic shape memory alloys processed by Severe Plastic Deformation"* <u>A.E. Kompatscher</u>, C. Mangler, P. Müllner, T. Waitz
Invited Talk:	TMS 2012, Orlando, FL, USA: *"Ultrafine-Grained Shape Memory Alloys"* <u>T. Waitz</u>, C. Mangler, G. Steiner, A.E. Kompatscher, M. Peterlechner, W. Pranger, T. Antretter, F.D. Fischer, P. Müllner
Invited Talk:	CIMTEC 2012, Montecatini Terme, ITA: *"Nanostructured Shape Memory Alloys: Processing, Martensitic Phase Transformations, Properties"* <u>T. Waitz</u>, C. Mangler, G. Steiner, A.E. Kompatscher, M. Peterlechner, T. Antretter, F.D. Fischer, P. Müllner
Talk:	ESOMAT 2012, St. Petersburg, RUS; abstract accepted for oral presentation: *"Ni-Ma-Ga Alloys processed by severe plastic deformation"* C. Mangler, A.E. Kompatscher, N. Kucza, P. Müllner, <u>T. Waitz</u>

Language Skills

Native:	German
Fluent:	English
Good:	French
Basic:	Spanish

Computer Skills

Scientific Programs:	LabVIEW, Origin, QtiPlot, Gatan Digital Micrograph, Netzsch Proteus Analysis
Markup Languages:	LaTeX, HTML
Design & Image Processing:	Inkscape, Adobe Photoshop, GIMP
Operating Systems:	MacOS, Ubuntu, MS Windows